

Deconstructing Intraocular Pressure: A Non-invasive Multi-Stage Probabilistic Inverse Framework

Md Rezwan Jaher

Independent Researcher, Dhaka, Bangladesh
rezwan.plabon@gmail.com

Abul Mukid Mohammad Mukaddes, A. B. M. Abdul Malek

Department of Industrial & Production Engineering, Shahjalal University of Science and Technology, Sylhet, Bangladesh
mukaddes-ipe@sust.edu, bashar@sust.edu

Abstract

Many critical healthcare decisions are challenged by the inability to measure key underlying parameters. Glaucoma, a leading cause of irreversible blindness driven by elevated intraocular pressure (IOP), provides a stark example. The primary determinant of IOP, a tissue property called trabecular meshwork permeability, cannot be measured *in vivo*, forcing clinicians to depend on indirect surrogates. This clinical challenge is compounded by a broader computational one: developing predictive models for such ill-posed inverse problems is hindered by a lack of ground-truth data and prohibitive cost of large-scale, high-fidelity simulations. We address both challenges with an end-to-end framework to non-invasively estimate unmeasurable variables from sparse, routine data. Our approach combines a multi-stage artificial intelligence architecture to functionally separate the problem; a novel data generation strategy we term PCDS that obviates the need for hundreds of thousands of costly simulations, reducing the effective computational time from years to hours; and a Bayesian engine to quantify predictive uncertainty. Our framework deconstructs a single IOP measurement into its fundamental components, yielding estimates for the unmeasurable tissue permeability and a patient's outflow facility. Validation against diverse clinical data confirmed the framework's high fidelity. Our non-invasive estimates of outflow facility achieved excellent agreement with state-of-the-art tonography, showing near-zero bias and precision comparable to direct physical instruments. Furthermore, the newly derived permeability biomarker demonstrates high accuracy in stratifying clinical cohorts by disease risk, highlighting its diagnostic potential. This work delivers a computational tool for clinical decision support by providing a complete, probabilistic profile of a patient's condition. This profile visualizes the entire distribution of plausible hydrodynamic states consistent with routine inputs (age and IOP), offering a holistic view unattainable with current methods and democratizing access to advanced diagnostics. More broadly, our framework establishes a generalizable blueprint for solving similar inverse problems in other data-scarce, computationally-intensive domains.

Key words: Glaucoma, Inverse Problem, Physics-Informed Machine Learning, Uncertainty Quantification, Simulation

1 Introduction

Glaucoma, a leading cause of irreversible blindness projected to affect over 110 million people by 2040 (Quigley and Broman 2006, Tham et al. 2014), is defined by progressive optic nerve damage, for which elevated intraocular pressure (IOP) is the primary modifiable risk factor (Foster et al. 2002). Consequently, lowering IOP is the only clinically proven treatment to arrest the progression of the disease. (Weinreb et al. 2014, European Glaucoma Society 2021). The homeostatic regulation of IOP is governed by the trabecular meshwork (TM), a porous tissue whose intrinsic effective permeability (K_{TM}) dictates resistance to aqueous humor outflow (Maepea and Bill 1989). In open-angle glaucoma (OAG), pathologically reduced K_{TM} is the principal cause of the sustained IOP elevation that drives optic neuropathy (Kaufman 2011, Acott and Kelley 2008). However, this fundamental biophysical property remains unmeasurable *in vivo* (Ethier et al. 1986), forcing clinical assessment to depend on indirect surrogates, principally outflow facility (OF).

Yet, OF provides an incomplete and often confounding picture of TM health. As a lumped parameter, it cannot distinguish an intrinsic permeability defect from other anatomical or physiological variations; for instance, a given OF value can reflect a healthy TM in one patient yet signify pathology in another with higher aqueous production. Furthermore, its measurement is fraught with compromise: tonography is practical but confounded by non-trabecular pathways and ocular biomechanics, whereas techniques like fluorophotometry are too invasive and time-consuming for routine clinical use (Toris et al. 2021). This leaves a critical clinical gap. With the primary biomarker of outflow resistance unmeasurable *in vivo*, and other key hydrodynamic parameters such as aqueous humor inflow (Q_{AH}), uveoscleral outflow (F_u), and episcleral venous pressure (EVP) also not routinely measured, interpreting the clinical meaning of a single IOP measurement becomes a severely underdetermined problem (Figure 1).

This clinical data gap is compounded by a broader computational challenge: a lack of ground-truth data necessitates reliance on high-fidelity simulations, yet generating the vast number of unique, patient-specific geometries required to capture true anatomical variability is computationally intractable, forcing most models to rely on idealized representations.

To address these coupled clinical and computational challenges, we propose an end-to-end framework that renders the underdetermined inverse problem tractable by architecturally deconstructing it according to its underlying physics. Conventional outflow through the trabecular meshwork is a form of flow through a porous medium, a process governed by Darcy’s Law. This physical principle mathematically separates the impact of intrinsic tissue permeability from the macroscopic geometry of the flow path, providing a natural blueprint for our multi-stage architecture (Figure 2). The first stage is designed to learn the universal biophysics by isolating the intrinsic permeability (K_{TM}). In computational science, learning from such computationally expensive,

first-principles simulations is often addressed by developing surrogate models, or metamodels, to emulate the system’s behavior (Russell and Martin 2006). Our first stage artificial intelligence (AI) solver is a direct implementation of this concept; it acts as a high-fidelity, physics-informed surrogate, trained on the dataset generated from our Finite Element (FE) simulations. The second stage then addresses patient-specificity by learning an effective geometric factor (G) that acts as a bridge between the idealized FE model and the complexities of real-world patient variability. To enable the training of this calibration bridge, we introduce our core methodological contribution: a novel data generation strategy we term Physics-Calibrated Data Scaling (PCDS). This strategy generates a massive, clinically-anchored dataset by calibrating an efficient analytical surrogate model against our high-fidelity FE model. Using this dataset, which includes the permeability estimate from the Stage 1 AI Solver as an important predictive feature, we can train the second stage to solve for the patient-specific effective geometric term. The entire probabilistic framework is essential for formally constraining the solution space using plausible physiological priors, providing a mechanism for robust Bayesian inference and the formal quantification of uncertainty (Adrian et al. 1995).

From this integrated foundation, our framework delivers three key methodological advances. First, our approach provides, to our knowledge, the first computationally derived *in vivo* estimates of the latent, unmeasurable K_{TM} , establishing a direct, mechanistic link between an IOP measurement and its root cause. Second, it delivers the first computational tool for estimating outflow facility, the current clinical gold standard, from routine clinical inputs alone, achieving a fidelity comparable to direct physical measurement while being independent of specialized equipment. Finally, the framework’s probabilistic engine provides a mechanism for comprehensive uncertainty quantification, yielding a full profile of the patient’s hydrodynamic state. This profile serves as a potential decision support tool through which clinicians can visualize the complex relationships among all underlying physiological parameters, quantitatively assess predictive uncertainty, and obtain a more mechanistic understanding of an individual’s condition. This work establishes the foundation for a shift from surrogate-based monitoring to a direct, data-driven, and mechanistic assessment of glaucoma, and the core methodological blueprint offers a potential strategy for a broader class of data-scarce, ill-posed inverse problems.

2 Methods

Here, we provide the detailed methodology for the development and validation of our physics-informed, multi-stage probabilistic inverse framework. We first present the overall framework architecture and rationale. We then describe the computational model development used to generate the foundational training data, including the FE geometry, governing physical equations, and numerical implementation. Next, we detail the formulation of the supervised learning tasks and the

Figure 1. The clinical problem and conceptual rationale for a physics-informed inverse solution. (a) Schematic of aqueous humor drainage in healthy versus glaucomatous eyes, adapted from [Servier](#), licensed under [CC-BY 3.0](#). (b) Key hydrodynamic parameters, measurement gaps, and limitations of current models. * Denotes a formulation adapted to emphasize key physical relationships (c) Overview of methodological challenges and our proposed solution.

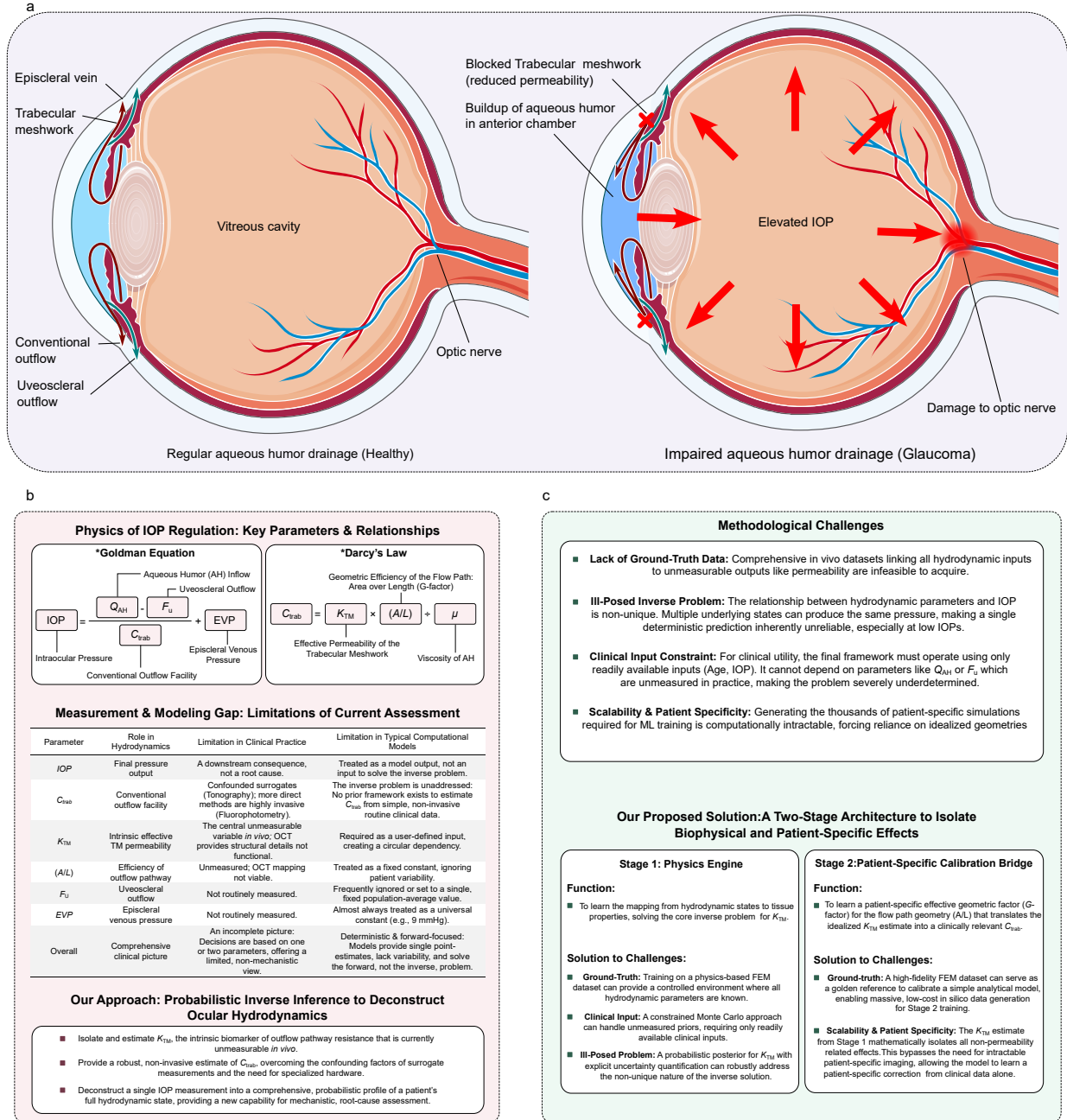
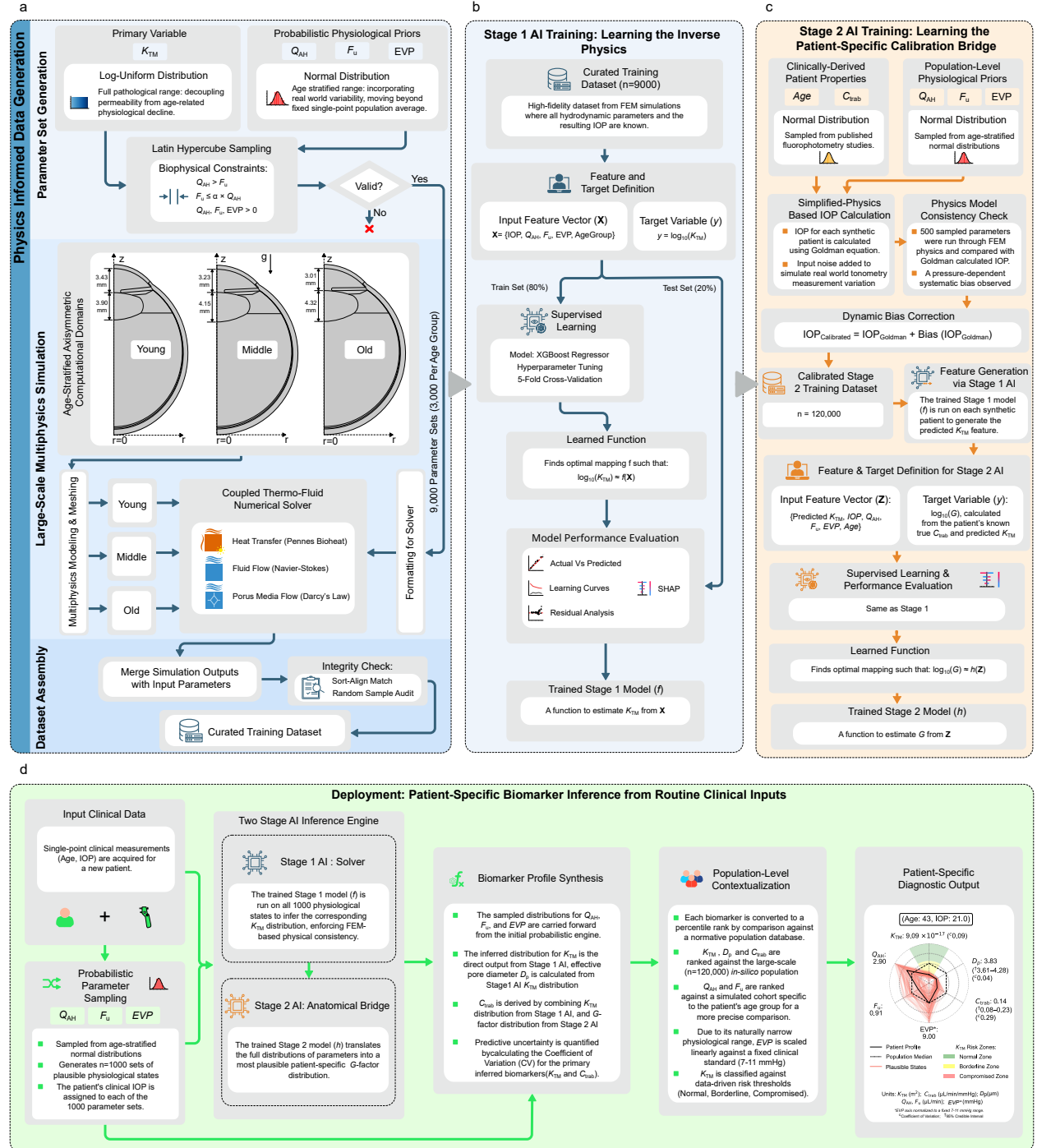


Figure 2. Methodological framework for the multi-stage probabilistic inverse model. (a) The physics-informed data generation pipeline, using a multiphysics finite element method solver to create a high-fidelity ground-truth dataset. (b) The Stage 1 AI training pipeline, where an XGBoost regressor learns the core inverse physics. (c) The Stage 2 AI training pipeline, where a second model learns a patient-specific calibration factor from a clinically-informed *in silico* dataset. (d) The clinical deployment engine, which uses the trained two-stage model for patient-specific probabilistic inference.



training of the machine learning models for biomarker inference. This is followed by a description of the clinical and *in silico* cohorts curated for validation. Finally, we outline the statistical methods employed for all analyses.

2.1 A Multi-Scale Computational Framework: Architecture and Rationale

Our approach to deconstructing IOP is a multi-scale computational framework designed to solve the inverse problem of estimating key unmeasurable parameters like K_{TM} from routine clinical inputs. A central innovation is our two-stage AI architecture, which is explicitly grounded in the physics of fluid dynamics and is visualized in Figure 1 and 2. The key function of this design is to decouple conventional outflow facility (C_{trab}) into two distinct, solvable components: an intrinsic effective tissue permeability, K_{TM} and a patient-specific effective geometry factor, G .

A central challenge in building a predictive model from first principles is bridging the gap between an idealized computational domain and the complex anatomy of individual subjects. While a physics-based FE model is computationally tractable, its flow path is necessarily an idealized simplification. A single-stage AI trained on such data would inevitably confound two distinct effects: the fundamental biophysics relating K_{TM} to IOP and the patient-specific variations inherent to *in vivo* physiology. Moreover, while all governing hydrodynamic equations link these variables, they cannot be solved directly for an individual patient. With only IOP known *in vivo*, the system remains severely underdetermined.

The key to a tractable solution lies in the physical definition of outflow facility. The physical basis for our two-stage separation is the composite nature of C_{trab} , which is a function of both K_{TM} and the macroscopic geometry of the outflow pathway. The governing physics of flow through the TM are described by Darcy’s Law, which relates the total aqueous flow through the TM (Q_{TM}) to the pressure drop across it (ΔP), its intrinsic permeability (K_{TM}), and its geometry, represented by an area-to-length ratio (A/L):

$$Q_{\text{TM}} = K_{\text{TM}} \cdot \left(\frac{A}{L} \right) \cdot \left(\frac{\Delta P}{\mu} \right) \quad (1)$$

By definition, C_{trab} relates this same flow to the pressure drop:

$$C_{\text{trab}} = \frac{Q_{\text{TM}}}{\Delta P} \quad (2)$$

Combining these principles reveals that C_{trab} is a composite of intrinsic permeability and macroscopic geometry:

$$C_{\text{trab}} = K_{\text{TM}} \cdot \left(\frac{A}{L} \right) \cdot \left(\frac{1}{\mu} \right) \quad (3)$$

where μ is the dynamic viscosity of aqueous humor.

This physical decomposition provides the blueprint for our solution. Our two-stage AI is therefore designed to solve this underdetermined problem by functionally separating and solving for these components. The first stage, the *AI Solver*, is trained on high-fidelity physics simulations to learn the complex, non-linear relationship between a full hydrodynamic state and the resulting K_{TM} . The second stage, the Patient-Specific Calibration Bridge, is then trained on a large-scale, clinically-informed dataset to learn a patient-specific correction, which is embodied as an effective anatomical geometry factor (G -factor, representing A/L). This principled, two-step process is what allows the framework to deconstruct the system and provide a robust, mechanistically interpretable assessment from a single IOP measurement.

The successful training of this second stage, however, required a large-scale dataset that was simultaneously scalable, physically rigorous, and, critically, robust to the realities of clinical data. To meet these competing demands, we developed our novel hybrid data generation strategy that we term PCDS. This strategy enables the creation of massive, robust datasets by uniquely combining three principles: (1) Clinical Anchoring, where we ground the dataset in reality by sampling target variables (e.g., outflow facility) from real clinical *in vivo* data distributions; (2) Scalability, achieved by leveraging a computationally efficient surrogate model (the Goldman equation) for large-scale synthetic patient generation; and (3) Physical Fidelity, ensured by using our high-fidelity physics model as a reference to dynamically calibrate and correct for the known systematic biases of the simpler surrogate. To ensure the final model is resilient to real-world imperfections, we deliberately inject realistic measurement noise into the IOP inputs during this process. The PCDS methodology thereby yields a final training set that is computationally scalable, physically consistent, and robust for clinical deployment. The entire framework, from patient input to diagnostic output, is formalized in Algorithm 1.

2.2 Computational Model Development for Stage 1 Data Generation

The high-fidelity ground-truth dataset for the Stage 1 AI Solver was generated from a comprehensive two-dimensional (2D) axisymmetric FE model of the human eye. The model’s geometry was based on anatomically-averaged dimensions from established literature (Lim et al. 1992, Dubbelman et al. 2002, Karampatzakis and Samaras 2010, Crowder and Ervin 2013, Ng et al. 2012), with the 2D representation chosen to balance biophysical fidelity with computational feasibility for a large-scale simulation campaign. The model simulated coupled heat transfer and fluid dynamics using established governing equations, including the Pennes bioheat equation, Navier-Stokes equations, and Darcy’s Law (Pennes 1998, Mukaddes et al. 2018, Karampatzakis and Samaras 2010, Crowder and Ervin 2013, Ng et al. 2012, Bhandari et al. 2020, Rahman et al. 2022, Lin and Yuan 2010, Ooi and Ng 2008, Murphy et al. 1992, Merchant and Heys 2008). All model inputs—including physically

Algorithm 1 Patient-Specific Hydrodynamic Profiling Framework

1. **Input:** Patient Age Age_p , Intraocular Pressure IOP_p
 2. **Output:** Synthesized profile with posterior distributions for $\{K_{TM}, G, C_{trab}, D_p\}$ and constrained prior distributions for $\{Q_{AH}, F_u, EVP\}$
 3. Generate $N = 1000$ plausible hydrodynamic state vectors $\{\mathbf{X}_i\}_{i=1}^N$ by sampling physiological priors $\{Q_{AH}, F_u, EVP\}_i$ from age-stratified distributions $P(Age_p)$.
 4. For each state i , set $\mathbf{X}_i = \{IOP_p, Q_{AH,i}, F_{u,i}, EVP_i, Age_p\}$.
 5. **for** $i = 1 \rightarrow N$ **do**
 6. Infer permeability $K_{TM,i} \leftarrow AISolver(\mathbf{X}_i)$.
 7. Construct feature vector $\mathbf{Z}_i = \{K_{TM,i}, \mathbf{X}_i\}$.
 8. Infer geometry factor $G_i \leftarrow PatientSpecificCalibrationBridge(\mathbf{Z}_i)$.
 9. **end for**
 10. Synthesize full posterior distributions for K_{TM} from $\{K_{TM,i}\}_{i=1}^N$ and G from $\{G_i\}_{i=1}^N$.
 11. Derive posterior for C_{trab} by applying Equation (3) to the full distributions of K_{TM} and G .
 12. Derive posterior for D_p from the K_{TM} distribution using Equation (10) and age-dependent porosity $\varepsilon(Age_p)$.
 13. **return** All posterior and constrained prior distributions.
-

realistic boundary conditions, static thermophysical properties, and age-stratified probabilistic priors for key hydrodynamic parameters (Q_{AH} , F_u , and EVP) were derived from established clinical and experimental data (Ooi and Ng 2008, Gokul et al. 2014, Ströher et al. 2020, Ng et al. 2012, Toris et al. 2021, 1999, Guillon and Maïssa 2010, Khanal et al. 2019, Emeterio Nateras et al. 2014, Hirata 2007, Hirata et al. 2007). A constrained rejection sampling protocol ensured physiological plausibility of the sampled priors. The coupled governing equations were solved using commercial finite element software (COMSOL Multiphysics®, v6.3, COMSOL AB, Stockholm, Sweden), with a mesh convergence study confirming a stable, mesh-independent solution. Full details of the model’s implementation are provided in Supplementary Note 1.

2.3 Physics-informed machine learning framework

2.3.1 Formulation of the supervised learning tasks.

The estimation of key hydrodynamic parameters is formulated as two distinct supervised learning tasks. The first stage learns the inverse physics of the outflow system via a mapping function, f , that predicts the log-transformed K_{TM} from a vector of known hydrodynamic state variables, \mathbf{X} (Figure 2b):

$$\log_{10}(K_{\text{TM}}) \approx f(\mathbf{X}) \quad (4)$$

$$\mathbf{X} = \{\text{IOP}, Q_{\text{AH}}, F_u, \text{EVP}, \text{AgeGroup}\} \quad (5)$$

where AgeGroup is a categorical variable (Young, Middle, Old) determining the age-specific FE model geometry and physiological priors.

The second stage learns the patient-specific anatomical correction via a mapping function, h , that predicts the log-transformed anatomical geometry factor (G) from a feature vector, \mathbf{Z} :

$$\log_{10}(G) \approx h(\mathbf{Z}) \quad (6)$$

$$\mathbf{Z} = \{\text{Predicted } K_{\text{TM}}, \text{IOP}, Q_{\text{AH}}, F_u, \text{EVP}, \text{Age}\} \quad (7)$$

where Predicted K_{TM} is the estimate from the Stage 1 model (f), and Age is the patient's continuous numerical age.

For both tasks, we used tuned XGBoost regressors, trained on an 80/20 train/test split of their respective datasets with hyperparameters optimized via 5-fold cross-validated randomized search. Model fidelity was rigorously assessed on the held-out test data (Supplementary Note 4, Figure S4), and the physical plausibility of the learned relationships was confirmed using SHapley Additive exPlanations (SHAP) (Lundberg and Lee 2017).

2.3.2 Stage 1: AI Solver development and training.

The AI Solver was trained to learn the inverse physics of the outflow system using the high-fidelity dataset ($n = 9,000$) generated from our 2D axisymmetric FE model. This dataset provides a direct mapping from a comprehensive set of known hydrodynamic state variables (IOP, Q_{AH} , F_u , EVP, AgeGroup) to the ground-truth K_{TM} . To ensure the dataset robustly captured the underlying physics, we employed Latin Hypercube Sampling and explicitly decoupled K_{TM} from age-related physiological decline during the sampling process. A tuned XGBoost regressor (Chen and Guestrin 2016) was selected for the primary task of K_{TM} estimation, as it offered a superior balance of predictive performance, computational efficiency, and model parsimony compared to other evaluated algorithms (Supplementary Table S7).

2.4 Stage 2: Patient-Specific Calibration Bridge development and training.

Training the Stage 2 Patient-Specific Calibration Bridge required a large-scale, clinically-informed dataset, which was generated through our PCDS strategy. A brute-force approach, which would necessitate unique 3D patient-specific simulations (~ 4 hours/simulation), would be computationally intractable with an estimated multi-year runtime. Our PCDS strategy was therefore developed to make this task feasible.

First, a large synthetic population ($n = 120,000$) was generated by sampling from statistical distributions derived from clinical fluorophotometry studies (Toris et al. 2002, 2004, 1999, Fernandez-Barrientos et al. 2010). For each synthetic patient, an initial IOP was calculated using the clinical Goldman equation (Equation 8) with realistic measurement noise added.

$$\text{IOP}_{\text{Goldman}} = \frac{Q_{\text{AH}} - F_u}{C_{\text{trab}}} + \text{EVP} \quad (8)$$

To ensure physical consistency between the simplified surrogate and our high-fidelity FE model, we performed a direct comparison which revealed a systematic, pressure-dependent bias between the two models ($P = 1.30 \times 10^{-15}$). To create a physically robust training set, this known bias was corrected for using a dynamic bias correction function (Equation 9). This calibration step, which required an additional 500 FE simulations, took approximately two hours to complete.

$$\text{Bias}(\text{IOP}_{\text{Goldman}}) = 2.654 - 0.233 \times \text{IOP}_{\text{Goldman}} \quad (9)$$

The resulting calibrated IOP values ($\text{IOP}_{\text{calibrated}} = \text{IOP}_{\text{Goldman}} + \text{Bias}(\text{IOP}_{\text{Goldman}})$) were then used to generate the final feature set, which included the predicted K_{TM} from the trained Stage 1 AI Solver for each of the 120,000 entries. Consistent with the AI Solver, the Patient-Specific Calibration Bridge was implemented as a tuned XGBoost regressor, trained on this final, calibrated *in silico* dataset. The entire PCDS pipeline, including the initial Stage 1 simulation campaign (~ 6 hours) and this calibration step, reduced the total computational time from years to approximately eight hours, making the framework tractable.

2.5 Framework deployment and profile generation

The framework generates a patient-specific hydrodynamic profile from an individual’s age and a single IOP measurement (visualized in Figure 2d). First, it employs a constrained Monte Carlo simulation to generate 1,000 plausible hydrodynamic states by sampling from age-stratified priors (Q_{AH} , F_u , EVP) and applying a rejection sampling step to ensure biophysical plausibility (e.g., $Q_{\text{AH}} > F_u$). These 1,000 states are then processed by the trained two-stage AI engine to infer full posterior distributions for K_{TM} (Stage 1) and the anatomical G-factor (Stage 2), from which final distributions for C_{trab} and effective pore diameter (D_p) are derived. The final synthesized output is a radar plot (Figure 2d) that visualizes the complete patient-specific profile, including all parameters

and their predictive uncertainty, normalized against a reference population and contextualized with data-driven risk thresholds.

2.6 Clinical and *in silico* validation

2.6.1 Curation of clinical validation cohorts.

The framework’s performance was rigorously assessed against two distinct clinical cohorts curated from published literature. The first, a homogeneous paired-eye steroid-challenge cohort ($n = 19$), provided individual-level data for a well-controlled test of the framework’s sensitivity to pathological change and its predictive precision against a modern gold standard measurement instrument (FMAT-1) (Di Staso and Gaudio 2023). The second, a heterogeneous cohort compiled via systematic literature review to test generalizability, consisted of published summary data from 27 diverse clinical study groups (e.g., healthy, ocular hypertensive, and primary open-angle glaucoma patients; varied OF measurement techniques) across 22 publications (Toris et al. 2002, 2004, 1999, Sit et al. 2021, Gulati et al. 2017, Alaghband et al. 2019, Sit et al. 2008, Meyer et al. 1997, Liu et al. 2011, Hayashi et al. 1989, Fernandez-Barrientos et al. 2010, Kazemi et al. 2019, Hays et al. 2014, Goyal et al. 2010, Saito et al. 2001, Johnson et al. 2010, Gulati et al. 2012, Costagliola et al. 1995, Beltran-Agullo et al. 2011, Minckler et al. 2005, Grieshaber et al. 2010, Pandey and Sujata 2014). For each cohort, the reported summary statistics for age and IOP were used as inputs for subsequent analyses. A full list of the source studies is provided in Supplementary Table S10 and the full data is available at the public repository cited in the data and code availability statement (Section 5). To perform a non-circular validation of classification robustness, we generated synthetic populations ($n = 500$) from our clinical cohorts. Distinct from the cohorts used for threshold derivation discussed in the following section, these were generated for each study with available summary statistics by sampling Age and IOP from Normal distributions based on the cohort’s reported mean and standard deviation.

2.6.2 Derivation of Data-Driven Risk Thresholds.

Objective, data-driven thresholds for clinical risk stratification were derived via an *in silico* procedure. A large reference population ($n = 120,000$) was generated by sampling from clinical data distributions (Toris et al. 2002, Sit et al. 2008, Toris et al. 2004, Sit et al. 2021) of archetypal Normal ($n = 2$ cohorts) and Compromised ($n = 2$ cohorts) physiological states. Our framework was applied to predict a posterior median K_{TM} value for each synthetic individual. The Normal and Compromised thresholds were then defined as the 25th percentile of the Normal population’s K_{TM} distribution and the 75th percentile of the Compromised population’s K_{TM} distribution, respectively, with the intervening range defined as Borderline. These derived thresholds were then

validated against our full heterogeneous set of 27 clinical cohorts, for which ground-truth risk labels (Normal, Borderline, or Compromised) were assigned based on a systematic, rule-based system (Supplementary Note 6, Table S10). The ability of these thresholds to statistically separate the cohorts by diagnostic status and the resulting classification performance were then rigorously evaluated.

2.6.3 Analysis of steroid-induced changes and effective pore diameter.

To assess the framework’s sensitivity to pathological change, we analyzed the homogeneous paired-eye cohort. The statistical significance of the change in predicted K_{TM} between the untreated and steroid-treated conditions was determined using the two-sided Wilcoxon signed-rank test.

To provide a microstructural interpretation of the predicted K_{TM} , we translated it into an effective pore diameter, D_p . This was calculated using the Kozeny-Carman equation, a standard model for flow in porous media (Ferreira et al. 2014):

$$K_{\text{TM}} = \frac{D_p^2 \cdot \epsilon^3}{k \cdot (1 - \epsilon)^2} \quad (10)$$

where ϵ is the TM porosity and k is the Kozeny constant (typically ~ 150 – 180). For this study, we used age-dependent porosity values (ϵ) based on literature estimates (Ethier et al. 1986, Murphy et al. 1992) and a Kozeny constant (k) of 150. This equation was algebraically rearranged to solve for D_p . The resulting D_p represents a functionally equivalent hydraulic diameter and serves as an intuitive proxy for the microstructural state of the TM.

2.7 Statistical Analysis

We performed all analyses in Python (v3.12) using standard scientific libraries, including pandas (McKinney 2010), scikit-learn (Pedregosa et al. 2011), SciPy (Virtanen et al. 2020), XGBoost, and SHAP. The full analysis plan was defined prior to analysis, with a significance threshold of $P < 0.05$ and a global random seed of 123 set for reproducibility. We used the Spearman’s rank-correlation coefficient (ρ) to assess correlation between predicted K_{TM} and measured OF. Agreement between the framework’s estimated C_{trab} and clinically measured outflow facility values was quantified using Bland-Altman analysis, reporting the mean difference (bias) and 95% limits of agreement (LoA). For the homogeneous paired-eye cohort, we determined the statistical significance of changes in predicted K_{TM} with the two-sided Wilcoxon signed-rank test. To compare predicted K_{TM} values across the three independent risk groups (Normal, Borderline, Compromised), we used the Kruskal-Wallis H test, followed by pairwise Mann-Whitney U tests with Bonferroni correction. Finally, we evaluated risk classification performance using overall accuracy and the Cohen’s kappa coefficient (κ).

3 Results

Here, we first establish the predictive fidelity of the framework’s core AI engine on synthetic data. We then present a multi-faceted clinical validation of its primary outputs, demonstrating their utility in risk stratification and integrated ocular hydrodynamic profiling.

3.1 Fidelity of the biophysical learning engine

The computational core of our framework is the two-stage AI engine. To establish its foundational accuracy and confirm it learned physically plausible relationships, we evaluated its performance on held-out test sets from our synthetic data (Supplementary Note 4). A full suite of diagnostic tests for both AI stages is detailed in Supplementary Figure S4.

3.1.1 Stage 1: The AI Solver for inverse permeability prediction.

The Stage 1 AI Solver demonstrated solid predictive performance, accounting for 77% of the variance in the ground-truth $\log_{10}(K_{TM})$ values ($R^2 = 0.77$) on the held-out test set. A diagnostic analysis of the residuals revealed a pattern of heteroscedasticity, with predictive error increasing for higher values of K_{TM} . This behavior is an expected consequence of the underlying physics; at lower IOPs (associated with high K_{TM}), a wider range of hydrodynamic parameter combinations can produce the same pressure, making the inverse problem inherently more ambiguous. The model’s learning curve confirmed robust generalization without evidence of overfitting, and a SHAP analysis verified that the model had learned physically plausible relationships, correctly identifying IOP as the most influential feature.

3.1.2 Stage 2: The Patient-Specific Calibration Bridge for geometric factor prediction.

The Stage 2 model also demonstrated strong predictive performance, achieving a coefficient of determination (R^2) of 0.79 on the log-transformed test-set G -factor values. Unlike Stage 1, the residual plot was homoscedastic, with errors randomly distributed around zero and no discernible systematic bias. The model’s learning curve showed excellent generalization, with the cross-validation error consistently decreasing to approach the training error. SHAP analysis confirmed that the model learned a fundamental biophysical trade-off, correctly identifying the predicted K_{TM} as the most influential feature for estimating the G -factor. Together, these results establish that our two-stage AI engine is not only accurate and robust but also learns mechanistically interpretable relationships, providing a solid foundation for its clinical application.

3.2 Clinical validation and risk stratification.

Having established the fidelity of the AI engine on synthetic data, we next sought to assess its performance and clinical utility using *in vivo* human data. We performed a multi-faceted validation using several distinct cohorts to test three key aspects of the framework: the biophysical fidelity and pathological sensitivity of the K_{TM} biomarker, its utility in clinical risk stratification, and the agreement of the estimated C_{trab} with clinically measured OF.

3.2.1 Relation between predicted K_{TM} and measured outflow facility.

The framework’s primary biomarker, K_{TM} , was validated against its closest *in vivo* surrogate: clinically measured OF. This relationship was first tested for generalizability using our heterogeneous validation set ($n = 23$ cohorts). The framework’s K_{TM} estimates for this set showed a strong and statistically significant correlation with the measured OF values (Spearman’s $\rho = 0.891$; $P = 1.24 \times 10^{-8}$; Figure 3a). The correlation was even more pronounced in the more controlled conditions of a homogenous, paired-eye cohort ($n = 19$) (Di Staso and Gaudio 2023), reaching near-unity in the untreated eyes ($\rho = 0.972$; $P = 3.77 \times 10^{-12}$; Figure 3b) and remaining exceptionally strong in their steroid-treated fellow eyes ($\rho = 0.965$; $P = 2.71 \times 10^{-11}$; Figure 3c). Together, these findings confirm that our non-invasively inferred K_{TM} is a high-fidelity proxy for the hydraulic function of the conventional outflow pathway.

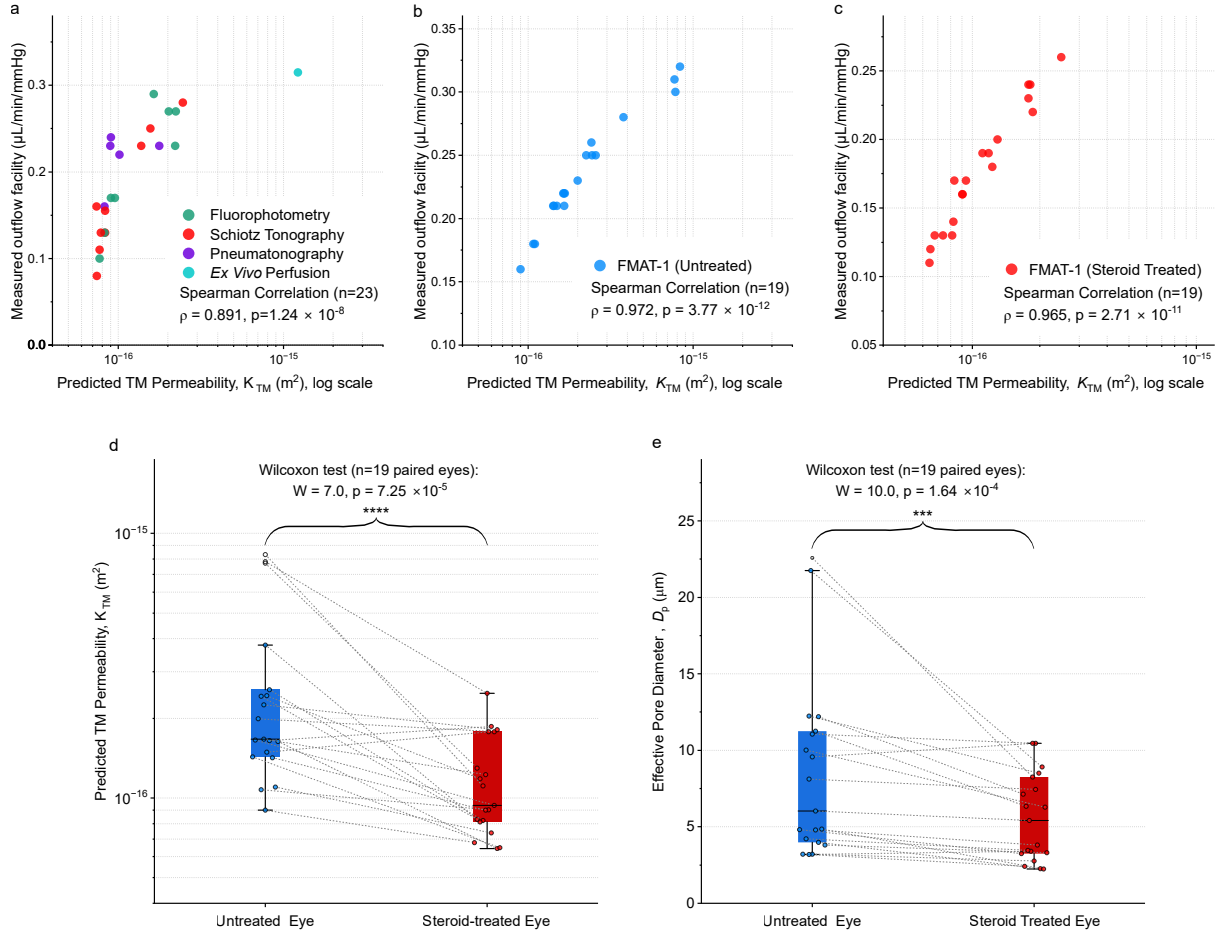
3.2.2 Sensitivity of K_{TM} to steroid-induced pathology.

The biomarker’s sensitivity to pathological change was tested using the paired-eye, steroid-challenge model (FMAT-1; $n=19$). The framework predicted a marked and statistically significant decrease in K_{TM} in the steroid-treated eyes compared to their untreated fellow eyes ($P = 7.25 \times 10^{-5}$, Wilcoxon signed-rank test; Figure 3d). To provide a microstructural correlate, K_{TM} was translated into an effective pore diameter (D_p), which revealed a consistent and significant reduction in pore size following steroid treatment ($P = 1.64 \times 10^{-4}$; Figure 3d). Importantly, the median D_p of the untreated eyes ($\sim 7 \mu m$) falls well within the experimentally reported range for the juxtacanalicular tissue region, the primary site of outflow resistance (Acott and Kelley 2008). This concordance provides strong external validation for the biophysical realism of the framework’s predictions.

3.2.3 K_{TM} as a biomarker for clinical risk stratification.

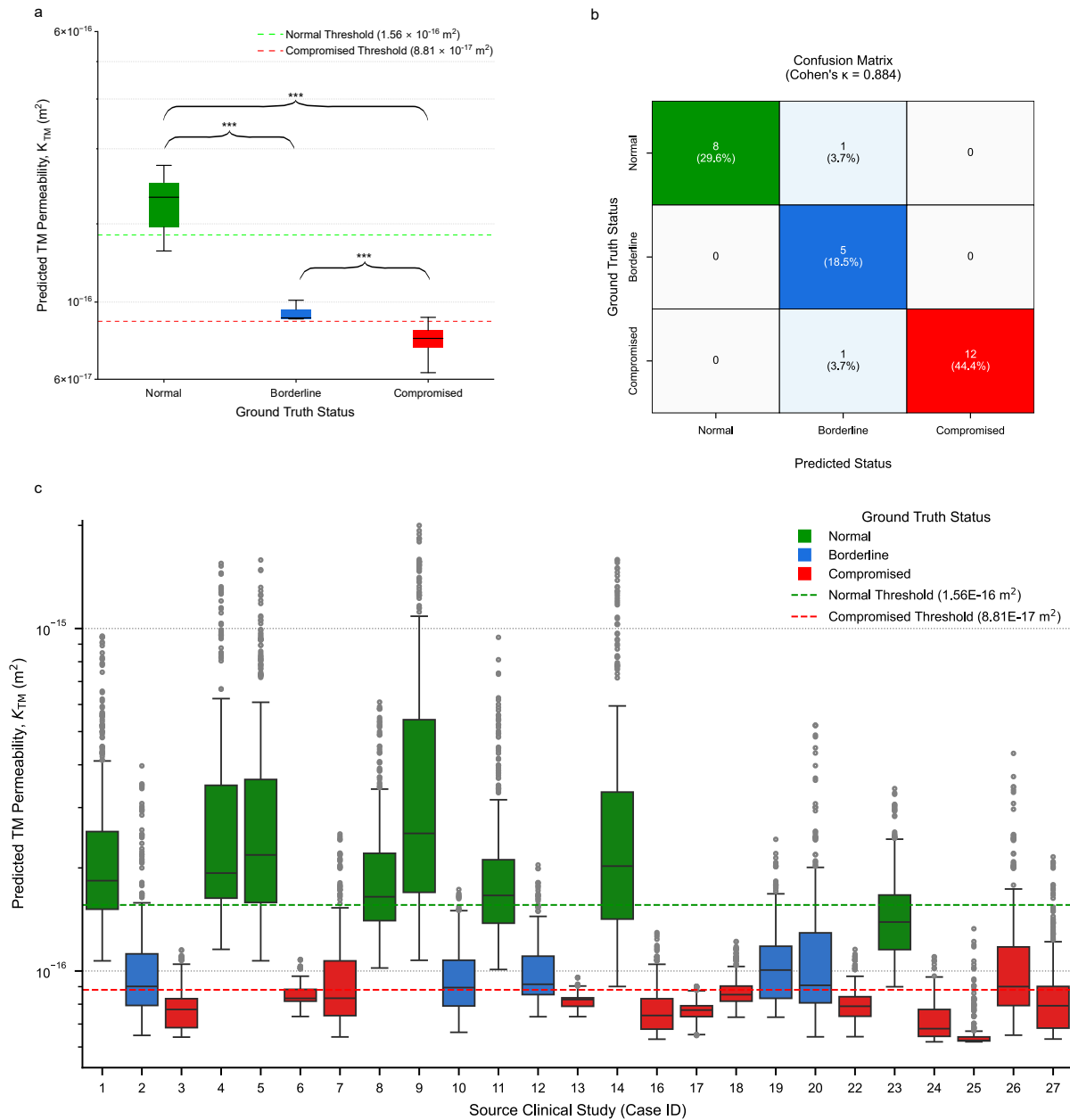
To test the ability of the K_{TM} biomarker to enable granular risk stratification, we evaluated its performance in classifying our heterogeneous set of 27 clinical cohorts according to their established diagnostic status. For each cohort, a representative K_{TM} value was predicted and then

Figure 3. Validation of inferred trabecular meshwork permeability (K_{TM}) against clinical data. a-c, Correlation between the posterior median predicted K_{TM} and clinically measured outflow facility (OF). Panel a shows data from a heterogeneous meta-analysis of 23 cohorts. Panels b and c show data from a homogeneous cohort ($n=19$) for untreated and steroid-treated eyes, respectively. d,e, Analysis of the biomarker's sensitivity to pathological change in a paired-eye, steroid-challenge model. Panel d shows the change in predicted K_{TM} following steroid treatment. Panel e shows the corresponding change in the derived effective pore diameter (D_p). Box plots show median, interquartile range, and 1.5x IQR whiskers.



classified into Normal, Borderline, or Compromised categories using our data-driven thresholds. The analysis confirmed that the cohort-level K_{TM} estimates for the three ground-truth risk groups were statistically distinct (Kruskal-Wallis test, $P = 2.20 \times 10^{-5}$; Figure 4a), with post-hoc pairwise tests confirming significant separation between all groups ($P < 0.001$). The classification performance demonstrated high diagnostic accuracy, with the framework correctly classifying 25 of the 27 cohorts and achieving a Cohen's κ of 0.884, indicating almost perfect agreement with the ground-truth status (Figure 4b). This robust classification was further confirmed at a population

Figure 4. Diagnostic performance and risk stratification using the predicted K_{TM} biomarker. Performance was evaluated against data-driven risk thresholds. a, Distribution of the posterior median predicted K_{TM} for 27 clinical cohorts, grouped by their ground-truth diagnostic status (Normal, Borderline, Compromised). Box plots show median, interquartile range, and 1.5x IQR whiskers. b, Confusion matrix of the classification performance for the 27 cohorts. c, Predicted K_{TM} distributions for simulated patient populations derived from each of the 27 source clinical studies, illustrating classification robustness at a population level.



level by generating new *in silico* populations for each cohort (Figure 4c).

3.2.4 Agreement between estimated and measured outflow facility.

The framework’s clinical translatability was further tested by its ability to accurately estimate C_{trab} . Generalizability was first assessed against our heterogeneous validation set ($n = 22$ cohorts), where the framework’s cohort-level estimates maintained low overall bias and reasonable agreement with measured OF summary data from diverse measurement techniques (mean difference = $-0.027 \mu\text{L}/\text{min}/\text{mmHg}$; 95% LoA $[-0.094, 0.041]$; Figure 5a). The framework’s precision was then benchmarked against state-of-the-art tonography from the homogenous FMAT-1 cohort, where it achieved near-zero bias and exceptionally tight limits of agreement for both untreated (mean difference = $0.011 \mu\text{L}/\text{min}/\text{mmHg}$; 95% LoA $[-0.019, 0.042]$; Figure 5b) and steroid-treated eyes (mean difference = $-0.013 \mu\text{L}/\text{min}/\text{mmHg}$; 95% LoA $[-0.061, 0.035]$; Figure 5c). A comprehensive statistical validation confirmed the high reliability of these findings (ICC [95% CI 0.690, 0.970] = 0.918 for untreated eyes; Supplementary Table S9). Remarkably, this level of precision approaches the reported test-retest reliability of tonography itself, suggesting our non-invasive method can achieve a fidelity comparable to direct physical measurement. Finally, to characterize the model’s predictive uncertainty, we visualized the full posterior distribution for each FMAT-1 patient (Figure 5d,e). This confirmed the low overall bias on a per-patient basis and, importantly, demonstrated the framework’s ability to express greater uncertainty for clinically atypical cases, a key strength of its probabilistic approach.

3.3 Integrated Ocular Hydrodynamic Profiling: Clinical Case Studies

The framework’s ultimate utility is its ability to synthesize all outputs into an integrated, patient-specific profile that deconstructs a single IOP measurement. This capability is illustrated through case studies from two distinct clinical scenarios (Figure 6). First, paired-eye analyses from the FMAT-1 cohort demonstrate the framework’s ability to identify the primary hydrodynamic mechanism of IOP elevation—a dramatic, isolated drop in K_{TM} and C_{trab} —providing a direct mechanistic insight unattainable with current methods (Figure 6a-d). Second, a six-visit longitudinal profile of a single OAG patient over a four-year period (Huang et al. 2023) shows the framework’s ability to track the dynamic evolution of TM health, capturing periods of both stability and decline (Figure 6e). This integrated, longitudinal profiling moves beyond static risk assessment, offering a powerful new tool for monitoring disease progression and potentially for titrating therapy based on direct, mechanistic feedback.

Figure 5. Validation of estimated conventional outflow facility (C_{trab}) against clinical measurements. a-c, Bland-Altman analysis comparing the framework's posterior median estimate of C_{trab} against clinically measured outflow facility for (a) a heterogeneous cohort and (b) a homogeneous cohort of untreated (c) and steroid-treated eyes. d,e, Probabilistic validation showing the full posterior distribution of the difference between the 1,000 probabilistic C_{trab} estimates and the single measured OF value for each patient in the untreated (d) and steroid-treated (e) conditions of the homogeneous cohort.

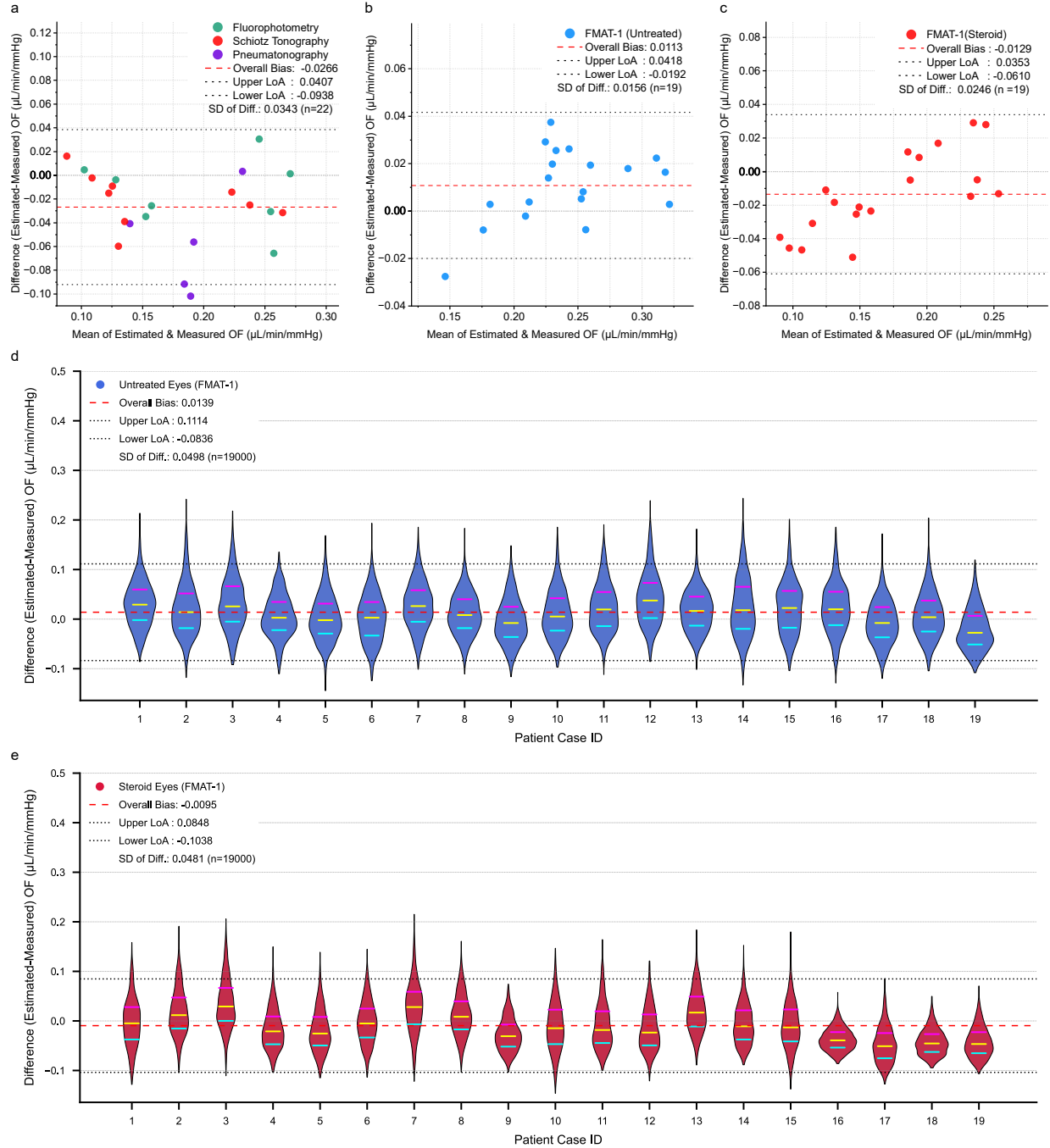
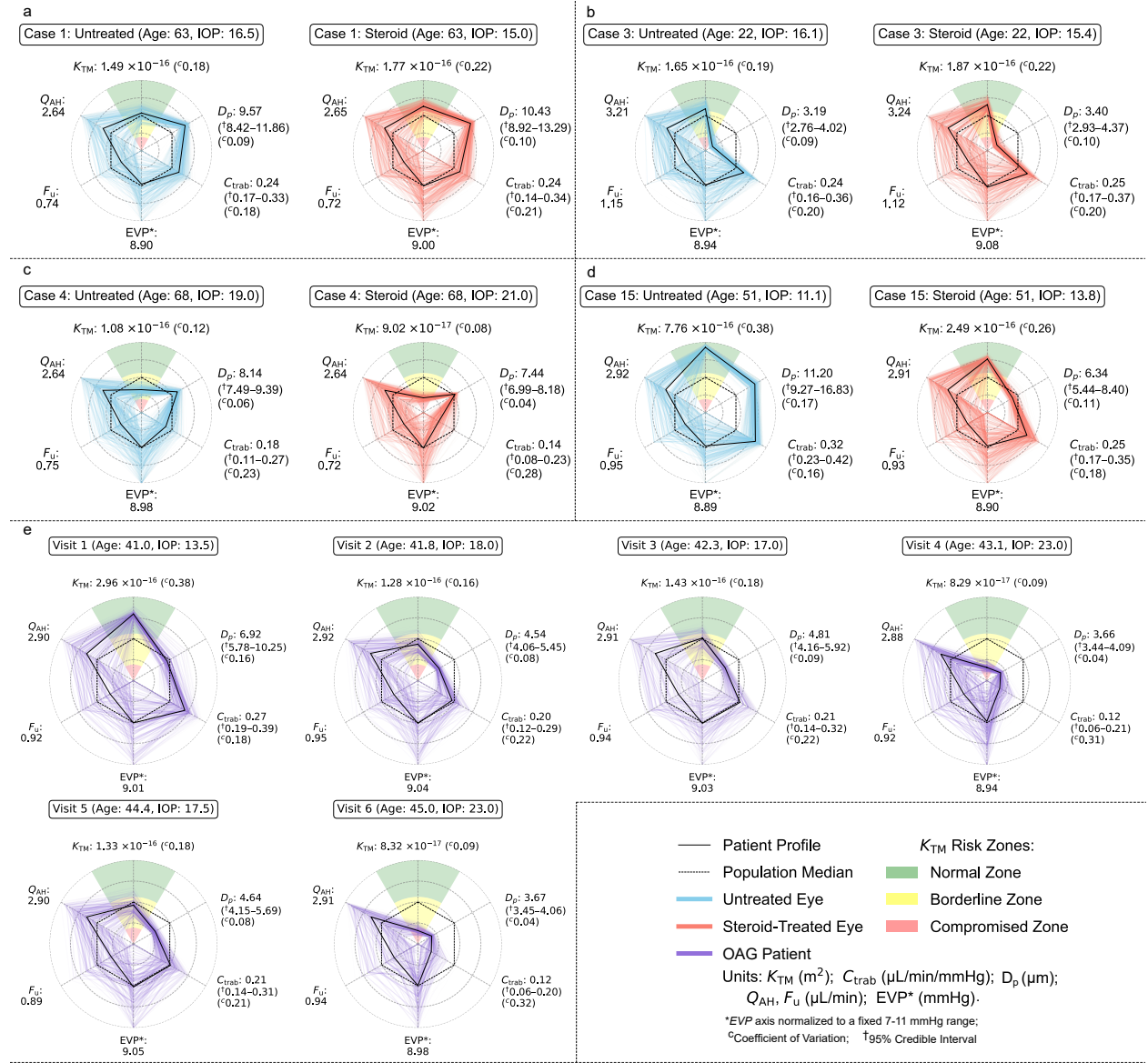


Figure 6. Patient-specific hydrodynamic profiles from clinical and longitudinal case studies. Each radar plot shows the full posterior distribution (faint lines), posterior median (solid line), and population median (dashed hexagon) for all hydrodynamic parameters. a-d, Paired-eye analyses from the FMAT-1 steroid-challenge cohort (Di Staso and Gaudio 2023), comparing untreated (blue) and steroid-treated (red) eyes. e, A six-visit longitudinal profile of a single open-angle glaucoma patient from the GRAPE cohort (Huang et al. 2023), tracking hydrodynamic changes over four years.



4 Discussion

This study introduces a computational framework that, to our knowledge, presents the first end-to-end solution for a challenging class of ill-posed inverse problems, such as the clinical problem of

glaucoma, characterized by data scarcity and the need for patient-specific inference. By leveraging a physics-informed AI engine, our approach deconstructs a single clinical measurement (IOP) into a complete, probabilistic profile of its underlying ocular hydrodynamics. In doing so, this work provides a direct, mechanistic alternative to simple surrogate measures, addressing a fundamental gap not only in glaucoma management, but also in the broader computational development of mechanistic models from sparse, real-world data.

The success of our framework is underpinned by key methodological innovations. The two-stage AI architecture is central to our approach, as it architecturally isolates the task of pure biophysical inference from that of patient-specific calibration. This deconstructionist design provides a generalizable blueprint for similar problems where system outputs are a composite of universal physical laws and individual-specific factors. This sophisticated architecture is made computationally tractable by our second core contribution, a novel data generation strategy termed PCDS. PCDS provides a blueprint for generating massive, physically-consistent training data by calibrating an efficient surrogate model against a small set of high-fidelity simulations, thereby overcoming the primary bottleneck in developing such physics-informed models.

The framework’s ability to accurately infer a latent, unmeasurable system parameter was demonstrated by the robust validation of the K_{TM} biomarker. The near-unity correlation with clinical surrogates (Figure 3a-c), combined with its pathological sensitivity in the steroid-induced glaucoma model (Figure 3d) and its high accuracy in stratifying potential clinical risk (Cohen’s $\kappa = 0.88$, Figure 4b), demonstrates that the framework successfully isolated the primary determinant of out-flow resistance. Furthermore, the framework’s utility as a data-driven decision support tool was established through its highly accurate, non-invasive estimate of C_{trab} . The model achieved near-zero bias and tight limits of agreement against state-of-the-art tonography (Figure 5b,c), with a level of fidelity comparable to the test-retest reliability of the physical measurement itself. Finally, the framework’s comprehensive uncertainty quantification moves beyond single point estimates to provide a full profile of all plausible hydrodynamic states consistent with the patient’s IOP, offering a holistic view of their physiological condition.

The framework’s current implementation incorporates several deliberate methodological trade-offs designed to prioritize end-to-end accuracy and clinical applicability. The underlying physics engine treats the trabecular meshwork as a homogenous porous medium, a necessary simplification of its complex microarchitecture. Consequently, the inferred K_{TM} represents an effective bulk permeability rather than a direct microscopic property. Similarly, the G -factor model, while validated as effective, functions as an empirical bridge between these idealized physics and *in vivo* complexity; the inferred G -factor should therefore be interpreted as an effective parameter rather than a pure anatomical quantity. This methodological trade-off, which prioritizes the end-to-end accuracy of the final C_{trab} estimate over the strict interpretational purity of intermediate

components, is crucial for the framework’s robustness. Most importantly, the validation presented here is retrospective. While performance against existing data is high, the framework’s definitive clinical utility awaits prospective evaluation.

5 Data and Code Availability

The Supplementary Information file contains additional details on the model development, validation, and sensitivity analyses. The complete source code, curated datasets, and trained models presented in this study have been archived in a Zenodo repository and are publicly available under the DOI: [10.5281/zenodo.17143276](https://doi.org/10.5281/zenodo.17143276).

References

- Acott TS, Kelley MJ (2008) Extracellular matrix in the trabecular meshwork. *Exp Eye Res* 86(4):543–61, ISSN 0014-4835, URL <http://dx.doi.org/10.1016/j.exer.2008.01.013>.
- Adrian ER, Geof HG, Judith EZ (1995) Inference from a deterministic population dynamics model for bowhead whales. *Journal of the American Statistical Association* 90(430):402–416, URL <http://dx.doi.org/10.1080/01621459.1995.10476529>.
- Alagband P, Baneke AJ, Galvis E, Madekurozwa M, Chu B, Stanford M, Overby D, Lim KS (2019) Aqueous humor dynamics in uveitic eyes. *Am J Ophthalmol* 208:347–355, ISSN 1879-1891, URL <http://dx.doi.org/10.1016/j.ajo.2019.08.018>.
- Beltran-Agullo L, Alagband P, Rashid S, Gosselin J, Obi A, Husain R, Lim KS (2011) Comparative human aqueous dynamics study between black and white subjects with glaucoma. *Invest Ophthalmol Vis Sci* 52(13):9425–30, ISSN 1552-5783, URL <http://dx.doi.org/10.1167/iovs.10-7130>.
- Bhandari A, Bansal A, Sinha N (2020) Effect of aging on heat transfer, fluid flow and drug transport in anterior human eye: A computational study. *J Control Release* 328:286–303, ISSN 1873-4995, URL <http://dx.doi.org/10.1016/j.jconrel.2020.08.044>.
- Chen T, Guestrin C (2016) Xgboost. URL <http://dx.doi.org/10.1145/2939672.2939785>.
- Costagliola C, Di Benedetto R, De Caprio L, Verde R, Mastropasqua L (1995) Effect of oral captopril (sq 14225) on intraocular pressure in man. *Eur J Ophthalmol* 5(1):19–25, ISSN 1120-6721, URL <http://dx.doi.org/10.1177/112067219500500104>.
- Crowder TR, Ervin VJ (2013) Numerical simulations of fluid pressure in the human eye. *Applied Mathematics and Computation* 219(24):11119–11133, ISSN 00963003, URL <http://dx.doi.org/10.1016/j.amc.2013.04.060>.
- Di Staso F, Gaudio PA (2023) Aqueous outflow facility after periocular triamcinolone injection: A prelim-

- inary evaluation of the falck medical applanation tonometer. *J Curr Glaucoma Pract* 17(4):197–204, ISSN 0974-0333, URL <http://dx.doi.org/10.5005/jp-journals-10078-1421>.
- Dubbelman M, Weeber HA, van der Heijde RG, Volker-Dieben HJ (2002) Radius and asphericity of the posterior corneal surface determined by corrected scheimpflug photography. *Acta Ophthalmol Scand* 80(4):379–83, ISSN 1395-3907, URL <http://dx.doi.org/10.1034/j.1600-0420.2002.800406.x>.
- Emeterio Nateras OS, Harrison JM, Muir ER, Zhang Y, Peng Q, Chalfin S, Gutierrez JE, Johnson DA, Kiel JW, Duong TQ (2014) Choroidal blood flow decreases with age: An mri study. *Current Eye Research* 39(10):1059–1067, ISSN 0271-3683, URL <http://dx.doi.org/10.3109/02713683.2014.892997>.
- Ethier CR, Kamm RD, Palaszewski BA, Johnson MC, Richardson TM (1986) Calculations of flow resistance in the juxtacanalicular meshwork. *Invest Ophthalmol Vis Sci* 27(12):1741–50, ISSN 0146-0404, URL <https://www.ncbi.nlm.nih.gov/pubmed/3793404>.
- European Glaucoma Society (2021) European glaucoma society terminology and guidelines for glaucoma, 5th edition. *Br J Ophthalmol* 105(Suppl 1):1–169, ISSN 1468-2079, URL <http://dx.doi.org/10.1136/bjophthalmol-2021-egsguidelines>.
- Fernandez-Barrientos Y, Garcia-Feijoo J, Martinez-de-la Casa JM, Pablo LE, Fernandez-Perez C, Garcia Sanchez J (2010) Fluorophotometric study of the effect of the glaukos trabecular microbypass stent on aqueous humor dynamics. *Invest Ophthalmol Vis Sci* 51(7):3327–32, ISSN 1552-5783, URL <http://dx.doi.org/10.1167/iovs.09-3972>.
- Ferreira JA, de Oliveira P, da Silva PM, Murta JN (2014) Numerical simulation of aqueous humor flow: From healthy to pathologic situations. *Applied Mathematics and Computation* 226:777–792, ISSN 00963003, URL <http://dx.doi.org/10.1016/j.amc.2013.10.070>.
- Foster PJ, Buhrmann R, Quigley HA, Johnson GJ (2002) The definition and classification of glaucoma in prevalence surveys. *Br J Ophthalmol* 86(2):238–42, ISSN 0007-1161, URL <http://dx.doi.org/10.1136/bjo.86.2.238>.
- Gokul KC, Gurung DB, Adhikary PR (2014) Thermal effects of eyelid in human eye temperature model. *Journal of applied mathematics & informatics* 32(5_6):649–663, ISSN 1598-5857, URL <http://dx.doi.org/10.14317/jami.2014.649>.
- Goyal S, Beltran-Agullo L, Rashid S, Shah SP, Nath R, Obi A, Lim KS (2010) Effect of primary selective laser trabeculoplasty on tonographic outflow facility: a randomised clinical trial. *Br J Ophthalmol* 94(11):1443–7, ISSN 1468-2079, URL <http://dx.doi.org/10.1136/bjo.2009.176024>.
- Grieshaber MC, Pienaar A, Olivier J, Stegmann R (2010) Clinical evaluation of the aqueous outflow system in primary open-angle glaucoma for canaloplasty. *Invest Ophthalmol Vis Sci* 51(3):1498–504, ISSN 1552-5783, URL <http://dx.doi.org/10.1167/iovs.09-4327>.
- Guillon M, Maïssa C (2010) Tear film evaporation—effect of age and gender. *Contact Lens and Anterior Eye* 33(4):171–175, ISSN 13670484, URL <http://dx.doi.org/10.1016/j.clae.2010.03.002>.

- Gulati V, Fan S, Gardner BJ, Havens SJ, Schaaf MT, Neely DG, Toris CB (2017) Mechanism of action of selective laser trabeculoplasty and predictors of response. *Invest Ophthalmol Vis Sci* 58(3):1462–1468, ISSN 1552-5783, URL <http://dx.doi.org/10.1167/iovs.16-20710>.
- Gulati V, Fan S, Zhao M, Maslonka MA, Gangahar C, Toris CB (2012) Diurnal and nocturnal variations in aqueous humor dynamics of patients with ocular hypertension undergoing medical therapy. *Arch Ophthalmol* 130(6):677–84, ISSN 1538-3601, URL <http://dx.doi.org/10.1001/archophthalmol.2011.2573>.
- Hayashi M, Yablonski ME, Novack GD (1989) Trabecular outflow facility determined by fluorophotometry in human subjects. *Exp Eye Res* 48(5):621–5, ISSN 0014-4835, URL [http://dx.doi.org/10.1016/0014-4835\(89\)90004-3](http://dx.doi.org/10.1016/0014-4835(89)90004-3).
- Hays CL, Gulati V, Fan S, Samuelson TW, Ahmed I, Toris CB (2014) Improvement in outflow facility by two novel microinvasive glaucoma surgery implants. *Invest Ophthalmol Vis Sci* 55(3):1893–900, ISSN 1552-5783, URL <http://dx.doi.org/10.1167/iovs.13-13353>.
- Hirata A (2007) Improved heat transfer modeling of the eye for electromagnetic wave exposures. *IEEE Trans Biomed Eng* 54(5):959–61, ISSN 0018-9294, URL <http://dx.doi.org/10.1109/TBME.2007.893492>.
- Hirata A, Watanabe S, Fujiwara O, Kojima M, Sasaki K, Shiozawa T (2007) Temperature elevation in the eye of anatomically based human head models for plane-wave exposures. *Physics in Medicine and Biology* 52(21):6389–6399, ISSN 0031-9155, URL <http://dx.doi.org/10.1088/0031-9155/52/21/003>.
- Huang X, Kong X, Shen Z, Ouyang J, Li Y, Jin K, Ye J (2023) Grape: A multi-modal dataset of longitudinal follow-up visual field and fundus images for glaucoma management. *Scientific Data* 10(1):520, ISSN 2052-4463, URL <http://dx.doi.org/10.1038/s41597-023-02424-4>.
- Johnson TV, Fan S, Zhan G, Camras CB, Toris CB (2010) Efficacy and mechanisms of intraocular pressure reduction with latanoprost and timolol in participants with ocular hypertension: a comparison of 1 and 6 weeks of treatment. *J Glaucoma* 19(6):356–64, ISSN 1057-0829, URL <http://dx.doi.org/10.1097/IJG.0b013e3181d12dd8>.
- Karampatzakis A, Samaras T (2010) Numerical model of heat transfer in the human eye with consideration of fluid dynamics of the aqueous humour. *Phys Med Biol* 55(19):5653–65, ISSN 1361-6560, URL <http://dx.doi.org/10.1088/0031-9155/55/19/003>.
- Kaufman PL (2011) Aqueous humor dynamics. Levin LA, Nilsson SFE, Ver Hoeve J, Wu S, Kaufman PL, Alm A, eds., *Adler's Physiology of the Eye*, chapter 7, 189–231 (Philadelphia, PA: Saunders Elsevier), 11 edition, ISBN 978-0-323-05714-1.
- Kazemi A, McLaren JW, Trese MGJ, Toris CB, Gulati V, Fan S, Reed DM, Kristoff T, Gilbert J, Moroi SE, Sit AJ (2019) Effect of timolol on aqueous humor outflow facility in healthy human eyes. *Am J Ophthalmol* 202:126–132, ISSN 1879-1891, URL <http://dx.doi.org/10.1016/j.ajo.2019.02.014>.
- Khanal S, Turnbull PRK, Vaghefi E, Phillips JR (2019) Repeatability of arterial spin labeling mri in measuring

- blood perfusion in the human eye. *J Magn Reson Imaging* 49(4):966–974, ISSN 1522-2586, URL <http://dx.doi.org/10.1002/jmri.26323>.
- Lim KJ, Hyung SM, Youn DH (1992) Ocular dimensions with aging in normal eyes. *Korean J Ophthalmol* 6(1):19–31, ISSN 1011-8942, URL <http://dx.doi.org/10.3341/kjo.1992.6.1.19>.
- Lin CW, Yuan F (2010) Numerical simulations of ethacrynic acid transport from precorneal region to trabecular meshwork. *Ann Biomed Eng* 38(3):935–44, ISSN 1573-9686, URL <http://dx.doi.org/10.1007/s10439-010-9947-z>.
- Liu H, Fan S, Gulati V, Camras LJ, Zhan G, Ghate D, Camras CB, Toris CB (2011) Aqueous humor dynamics during the day and night in healthy mature volunteers. *Arch Ophthalmol* 129(3):269–75, ISSN 1538-3601, URL <http://dx.doi.org/10.1001/archophthalmol.2011.4>.
- Lundberg SM, Lee SI (2017) A unified approach to interpreting model predictions. 4768–4777.
- Maepea O, Bill A (1989) The pressures in the episcleral veins, schlemm’s canal and the trabecular meshwork in monkeys: effects of changes in intraocular pressure. *Exp Eye Res* 49(4):645–63, ISSN 0014-4835, URL [http://dx.doi.org/10.1016/s0014-4835\(89\)80060-0](http://dx.doi.org/10.1016/s0014-4835(89)80060-0).
- McKinney W (2010) Data structures for statistical computing in python. URL <http://dx.doi.org/10.25080/Majora-92bf1922-00a>.
- Merchant BM, Heys JJ (2008) Effects of variable permeability on aqueous humor outflow. *Applied Mathematics and Computation* 196(1):371–380, ISSN 00963003, URL <http://dx.doi.org/10.1016/j.amc.2007.06.008>.
- Meyer MA, Savitt ML, Kopitas E (1997) The effect of phacoemulsification on aqueous outflow facility. *Ophthalmology* 104(8):1221–7, ISSN 0161-6420, URL [http://dx.doi.org/10.1016/s0161-6420\(97\)30154-7](http://dx.doi.org/10.1016/s0161-6420(97)30154-7).
- Minckler DS, Baerveldt G, Alfaro MR, Francis BA (2005) Clinical results with the trabectome for treatment of open-angle glaucoma. *Ophthalmology* 112(6):962–7, ISSN 1549-4713, URL <http://dx.doi.org/10.1016/j.ophtha.2004.12.043>.
- Mukaddes AMM, Jaher MR, Roy D, Shioya R (2018) A simulation study of bio-heat transfer in human skin under different burning conditions. *AIP Conference Proceedings* 1980(1), ISSN 0094-243X, URL <http://dx.doi.org/10.1063/1.5044338>.
- Murphy CG, Johnson M, Alvarado JA (1992) Juxtacanalicular tissue in pigmentary and primary open angle glaucoma. the hydrodynamic role of pigment and other constituents. *Arch Ophthalmol* 110(12):1779–85, ISSN 0003-9950, URL <http://dx.doi.org/10.1001/archophth.1992.01080240119043>.
- Ng E, Tan J, Acharya U, Suri J, eds. (2012) *Human Eye Imaging and Modeling* (Boca Raton, FL: CRC Press), 1st edition, URL <http://dx.doi.org/10.1201/b12081>.
- Ooi EH, Ng EY (2008) Simulation of aqueous humor hydrodynamics in human eye heat transfer. *Comput Biol Med* 38(2):252–62, ISSN 0010-4825, URL <http://dx.doi.org/10.1016/j.compbiomed.2007.10.007>.

- Pandey AN, Sujata S (2014) Study of long term structural and functional changes in medically controlled glaucoma. *Int J Ophthalmol* 7(1):128–32, ISSN 2222-3959, URL <http://dx.doi.org/10.3980/j.issn.2222-3959.2014.01.24>.
- Pedregosa F, Varoquaux G, Gramfort A, Michel V, Thirion B, Grisel O, Blondel M, Prettenhofer P, Weiss R, Dubourg V, Vanderplas J, Passos A, Cournapeau D, Brucher M, Perrot M, Duchesnay É (2011) Scikit-learn: Machine learning in python. *Journal of Machine Learning Research* 12(85):2825–2830, URL <http://jmlr.org/papers/v12/pedregosa11a.html>.
- Pennes HH (1998) Analysis of tissue and arterial blood temperatures in the resting human forearm. 1948. *J Appl Physiol* (1985) 85(1):5–34, ISSN 8750-7587, URL <http://dx.doi.org/10.1152/jappl.1998.85.1.5>.
- Quigley HA, Broman AT (2006) The number of people with glaucoma worldwide in 2010 and 2020. *Br J Ophthalmol* 90(3):262–7, ISSN 0007-1161, URL <http://dx.doi.org/10.1136/bjo.2005.081224>.
- Rahman MA, Rabbani M, Maruf MH, Islam A, Shihavuddin ASM (2022) Characterizing the aging process of the human eye: Tear evaporation, fluid dynamics, blood flow, and metabolism-based comparative study. *Biomed Res Int* 2022:2805402, ISSN 2314-6141, URL <http://dx.doi.org/10.1155/2022/2805402>.
- Russell RB, Martin M (2006) *Chapter 18 Metamodel-Based Simulation Optimization*, volume 13, 535–574 (Elsevier), URL [http://dx.doi.org/https://doi.org/10.1016/S0927-0507\(06\)13018-2](http://dx.doi.org/https://doi.org/10.1016/S0927-0507(06)13018-2).
- Saito M, Takano R, Shirato S (2001) Effects of latanoprost and unoprostone when used alone or in combination for open-angle glaucoma. *Am J Ophthalmol* 132(4):485–9, ISSN 0002-9394, URL [http://dx.doi.org/10.1016/s0002-9394\(01\)01096-0](http://dx.doi.org/10.1016/s0002-9394(01)01096-0).
- Sit AJ, Gupta D, Kazemi A, McKee H, Challa P, Liu KC, Lopez J, Kopczynski C, Heah T (2021) Netarsudil improves trabecular outflow facility in patients with primary open angle glaucoma or ocular hypertension: A phase 2 study. *Am J Ophthalmol* 226:262–269, ISSN 1879-1891, URL <http://dx.doi.org/10.1016/j.ajo.2021.01.019>.
- Sit AJ, Nau CB, McLaren JW, Johnson DH, Hodge D (2008) Circadian variation of aqueous dynamics in young healthy adults. *Invest Ophthalmol Vis Sci* 49(4):1473–9, ISSN 0146-0404, URL <http://dx.doi.org/10.1167/iovs.07-1139>.
- Ströher GR, de Andrade CR, Ströher GL (2020) Assessment of thermal models for human eye. *Heat and Mass Transfer* 56(7):2135–2143, ISSN 0947-7411, URL <http://dx.doi.org/10.1007/s00231-020-02845-6>.
- Tham YC, Li X, Wong TY, Quigley HA, Aung T, Cheng CY (2014) Global prevalence of glaucoma and projections of glaucoma burden through 2040: a systematic review and meta-analysis. *Ophthalmology* 121(11):2081–90, ISSN 1549-4713, URL <http://dx.doi.org/10.1016/j.ophtha.2014.05.013>.
- Toris CB, Gagrani M, Ghate D (2021) Current methods and new approaches to assess aqueous humor

- dynamics. *Expert Review of Ophthalmology* 16(3):139–160, ISSN 1746-9899, URL <http://dx.doi.org/10.1080/17469899.2021.1902308>.
- Toris CB, Koepsell SA, Yablonski ME, Camras CB (2002) Aqueous humor dynamics in ocular hypertensive patients. *J Glaucoma* 11(3):253–8, ISSN 1057-0829, URL <http://dx.doi.org/10.1097/00061198-200206000-00015>.
- Toris CB, Yablonski ME, Wang YL, Camras CB (1999) Aqueous humor dynamics in the aging human eye. *Am J Ophthalmol* 127(4):407–12, ISSN 0002-9394, URL [http://dx.doi.org/10.1016/s0002-9394\(98\)00436-x](http://dx.doi.org/10.1016/s0002-9394(98)00436-x).
- Toris CB, Zhan G, Camras CB (2004) Increase in outflow facility with unoprostone treatment in ocular hypertensive patients. *Arch Ophthalmol* 122(12):1782–7, ISSN 0003-9950, URL <http://dx.doi.org/10.1001/archophth.122.12.1782>.
- Virtanen P, Gommers R, Oliphant TE, Haberland M, Reddy T, Cournapeau D, et al. (2020) Scipy 1.0: fundamental algorithms for scientific computing in python. *Nature Methods* 17(3):261–272, ISSN 1548-7091, URL <http://dx.doi.org/10.1038/s41592-019-0686-2>.
- Weinreb RN, Aung T, Medeiros FA (2014) The pathophysiology and treatment of glaucoma: a review. *JAMA* 311(18):1901–11, ISSN 1538-3598, URL <http://dx.doi.org/10.1001/jama.2014.3192>.

Supplementary Information for:

Deconstructing Intraocular Pressure: A Non-invasive Multi-Stage Probabilistic Inverse Framework

Supplementary Note 1: Computational Model Development for Stage 1

The foundational training data for our Stage 1 AI Solver was generated using a comprehensive computational model of the human eye. This section details the Finite Element(FE) model geometry, the governing physical equations, the material properties and physiological priors, and the numerical implementation.

Model geometry.

A 2D axisymmetric FE model of the human eye with 11 distinct domains (Figure S1) was constructed based on anatomically-averaged dimensions derived from established literature (Table S1).

Table S1. Age-specific geometric dimensions of the eye model used for each simulation cohort. The values were derived and adapted from established ophthalmological literature (Lim et al. 1992, Dubbelman et al. 2002, Karampatzakis and Samaras 2010, Crowder and Ervin 2013, Ng et al. 2012).

Age group (years)	AC depth (mm)	Lens thickness (mm)	Axial length (mm)	Vertical length (mm)	Cornea radius (mm)
20–34 (Young)	3.43	3.90	24.22	23.09	7.902
34–55 (Middle)	3.23	4.15	23.90	22.76	7.822
>55 (Old)	3.01	4.32	23.87	22.76	7.822

Governing Physics and Equations.

Our computational FE model simulates coupled heat transfer and fluid dynamics. Heat transfer was modeled using the Pennes bioheat equation (Pennes 1998, Mukaddes et al. 2018, Karampatzakis

and Samaras 2010, Crowder and Ervin 2013, Ng et al. 2012, Bhandari et al. 2020, Rahman et al. 2022):

$$\rho c(\vec{v} \cdot \nabla T) + \nabla(-\alpha \nabla T) = Q_b + Q_m \quad (S1)$$

where ρ , c , and α are the domain-specific material properties of density, specific heat capacity, and thermal conductivity, respectively; T is temperature, \vec{v} is fluid velocity, and Q_m is metabolic heat generation. The blood perfusion term, Q_b , is defined as:

$$Q_b = \omega_b c_b \rho_b (T_b - T) \quad (S2)$$

where ω_b is the perfusion rate, and c_b , ρ_b , and T_b are the blood specific heat capacity, blood density, and arterial blood temperature, respectively.

Fluid dynamics for the aqueous humor were modeled as an incompressible, laminar, Newtonian fluid governed by the steady-state Navier-Stokes and continuity equations (Bhandari et al. 2020, Rahman et al. 2022, Lin and Yuan 2010, Ooi and Ng 2008):

$$\rho_{AH}(\vec{v} \cdot \nabla) \vec{v} = -\nabla p + \mu \nabla^2 \vec{v} + \vec{F} \quad (S3)$$

$$\nabla \cdot \vec{v} = 0 \quad (S4)$$

The Boussinesq buoyancy force term, $\vec{F} = \rho_{AH} \vec{g} \beta (T - T_{ref})$, models the effect of gravity on the thermally-stratified fluid and couples the thermal and fluid domains. Here, ρ_{AH} and μ are the aqueous humor density and dynamic viscosity; p and \vec{v} are the pressure and velocity fields; \vec{g} is the acceleration due to gravity; β is the coefficient of thermal expansion (set to 0.000337 K^{-1}); and T_{ref} is the reference temperature, set to the arterial blood temperature, T_b .

Flow through the porous trabecular meshwork (TM) was modeled using Darcy's Law (Rahman et al. 2022, Murphy et al. 1992, Merchant and Heys 2008):

$$\vec{v} = -\frac{K_{TM}}{\mu} \nabla p \quad (S5)$$

where the parameter K_{TM} is the intrinsic effective hydraulic permeability of the TM.

To isolate the conventional pathway, the largely pressure-insensitive uveoscleral outflow (F_u) was treated as a distributed mass sink. The effective trabecular inflow (Q_{TM}) was therefore defined as the total aqueous production (Q_{AH}) minus this sink:

$$Q_{TM} = Q_{AH} - F_u \quad (S6)$$

This Q_{TM} served as the inlet boundary condition for the simulation, with Q_{AH} and F_u drawn from their respective age-dependent physiological distributions.

Specification of thermal and fluid boundary conditions.

A complete set of boundary conditions was specified for the FE model's thermal and fluid domains (schematically depicted in Supplementary Figure S1).

For the thermal domain, a coupled convection, radiation, and evaporation condition was applied at the corneal surface (Ooi and Ng 2008, Gokul et al. 2014):

$$-\alpha \frac{\partial T}{\partial n} = h_{\text{amb}}(T - T_{\text{amb}}) + \sigma \epsilon (T^4 - T_{\text{amb}}^4) + E \quad (\text{S7})$$

where α is thermal conductivity, h_{amb} is the ambient convective coefficient, σ is the Stefan-Boltzmann constant, ϵ is emissivity, and E is evaporative heat loss. At the scleral boundary, convective heat exchange with orbital blood vessels was modeled (Gokul et al. 2014, Ströher et al. 2020):

$$-\alpha \frac{\partial T}{\partial n} = h_b(T - T_b) \quad (\text{S8})$$

where h_b is the blood convective coefficient and T_b is arterial blood temperature.

For the fluid domain, a parabolic inflow profile corresponding to the effective trabecular inflow (Q_{TM} from Equation S6) was prescribed as a total volumetric flow rate:

$$\int_{\partial\Omega_{\text{in}}} \vec{v} \cdot \vec{n} dS = Q_{\text{TM}} \quad (\text{S9})$$

At the distal outflow boundary of the TM, a constant pressure condition corresponding to the episcleral venous pressure (EVP) was set:

$$p = \text{EVP} \quad (\text{S10})$$

where EVP was sampled from its physiological distribution (Table S4). A no-slip condition ($\vec{v} = 0$) was applied to all solid-fluid boundaries (Equation S11). Continuity of pressure and normal velocity was enforced at the fluid-porous interface (Equations S12-S13), and a no-flow condition was applied at the TM side walls (Equation S14).

$$\vec{v} = 0 \quad (\text{S11})$$

$$p_{\text{AC}} = p_{\text{TM}} \quad (\text{S12})$$

$$\vec{v}_{\text{AC}} \cdot \vec{n} = \vec{v}_{\text{TM}} \cdot \vec{n} \quad (\text{S13})$$

$$\vec{v} \cdot \vec{n} = 0 \quad (\text{S14})$$

Material properties and physiological priors.

The thermophysical properties for each ocular tissue included in the model, such as thermal conductivity (α), heat capacity (c_p), and density (ρ), were defined based on established values from the literature, summarized in Table S2. These material constants were assumed to be uniform across the age groups. In contrast to the static material properties, a key feature of our modeling approach was the use of probabilistic sampling for the primary hydrodynamic parameters to reflect real-world biological variability. The age-dependent rates for tear evaporation, blood perfusion, and metabolic heat generation were sourced from prior experimental studies and are detailed in

Figure S1. Computational Model and Boundary Conditions. **a**, A 2D planar cross-section illustrating the model geometry. As we used an axisymmetric model, the computational domain consists of one half of this planar cross-section (the region where $r \geq 0$), which is revolved around the central vertical axis of symmetry. **b**, Non-uniform computational mesh with strategic refinement. **c-e**, Schematic of the thermal and fluid dynamics boundary conditions. **c**, Thermal conditions on the cornea and sclera. **d**, Fluid inflow and no-slip conditions. **e**, Detailed view of boundary conditions at the trabecular meshwork, including the pressure outlet and interface continuity.

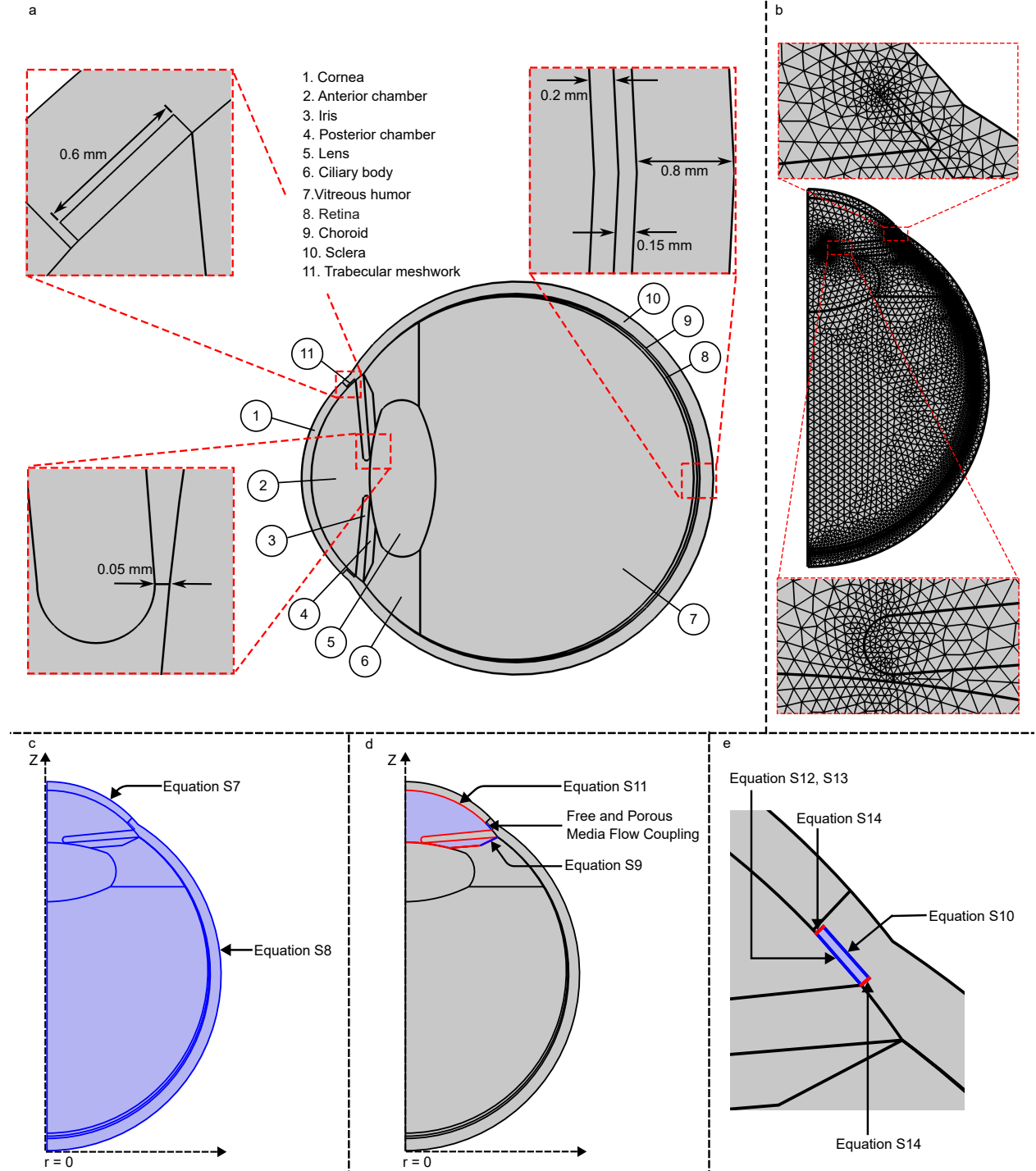


Table S3. For the core fluid dynamics, we sampled aqueous humor inflow (Q_{AH}) and uveoscleral outflow (F_u) from age-stratified normal distributions. We derived the mean and standard deviation for our Young and Old cohorts directly from the primary experimental data reported by [Toris et al. \(1999\)](#) and established the Middle cohort's parameters through logical interpolation. Similarly, we sampled episcleral venous pressure (EVP) from a single normal distribution, as it exhibits less age-dependency, basing its parameters on the consensus range synthesized in a comprehensive review by [Toris et al. \(2021\)](#). Specifically, we selected a mean of 1200 Pa (9.0 mmHg) to align with the center of the commonly reported physiological range, and a standard deviation of 200 Pa (~ 1.5 mmHg) to ensure that approximately 95% of the sampled population would fall within a plausible range of ~ 6 –12 mmHg, reflecting known physiological variability. We provide the specific parameters for all distributions in Table S4.

Table S2. Thermophysical properties of ocular tissues ([Ng et al. 2012](#)).

Property	Cornea	APC	Iris & Sclera	Lens	CB	VH	Retina	Choroid	TM
Thermal cond. (α) (W m ⁻¹ K ⁻¹)	0.58	0.58	1.0042	0.4	0.498	0.603	0.565	0.53	1.004
Heat capacity (c_p) (J kg ⁻¹ K ⁻¹)	4178	3997	3180	3000	3340	4178	3680	3840	3180
Density (ρ) (kg m ⁻³)	1050	996	1100	1050	1040	1000	1039	1060	1100

Abbreviations: APC, Anterior & Posterior Chamber; CB, Ciliary Body; VH, Vitreous Humor; TM, Trabecular Meshwork.

Table S3. Age-dependent physiological parameters for simulation.

Symbol	Unit	Young	Middle	Old	Source
E	W/m ²	27	41.8	50	Guillon and Maïssa (2010)
ω_b^a	ml/(ml · s)	0.01298	0.01038	0.00779	Khanal et al. (2019) ,
ω_b^b	ml/(ml · s)	9.26×10^{-3}	7.41×10^{-3}	5.93×10^{-3}	Emeterio Nateras et al. (2014)
Q_m^c	W/m ³	22000	17600	14080	Emeterio Nateras et al. (2014) ,
Q_m^d	W/m ³	10000	8000	6400	Hirata et al. (2007)
					Emeterio Nateras et al. (2014) ,
					Hirata et al. (2007)

E : Tear evaporation rate. ^a ω_b : Blood perfusion (Choroid, retina). ^b ω_b : Blood perfusion (Iris). ^c Q_m : Metabolism rate (Choroid, Retina). ^d Q_m : Metabolism rate (Iris).

Table S4. Age-dependent distribution parameters for hydrodynamic priors. All parameters were sampled from a Normal distribution.

Parameter	Symbol	Unit	Age Group	Mean	SD	Source
Aqueous Humor Inflow	Q_{AH}	m^3/s	Young	4.83×10^{-11}	1.50×10^{-11}	(Toris et al. 1999)
			Middle	4.33×10^{-11}	1.33×10^{-11}	\dagger (Toris et al. 1999)
			Old	4.00×10^{-11}	1.17×10^{-11}	(Toris et al. 1999)
Uveoscleral Outflow	F_u	m^3/s	Young	2.53×10^{-11}	1.35×10^{-11}	(Toris et al. 1999)
			Middle	2.17×10^{-11}	1.33×10^{-11}	\dagger (Toris et al. 1999)
			Old	1.83×10^{-11}	1.35×10^{-11}	(Toris et al. 1999)
Episcleral Venous Pressure	EVP	Pa	All	1200.0	200.0	\ddagger (Toris et al. 2021)

\dagger Value derived via interpolation. \ddagger Consensus value derived from literature review.

To maintain physiological plausibility, we constrained these sampled parameters using a rejection sampling protocol. We validated each generated parameter set to ensure, for example, that total inflow was greater than uveoscleral outflow ($Q_{AH} > F_u$) and that uveoscleral outflow did not exceed an age-dependent fraction of total inflow. This probabilistic and constrained sampling strategy was essential for generating a high-fidelity training dataset representative of the variability inherent in human physiology.

Numerical Solution and Mesh Convergence.

The coupled governing partial differential equations were solved using the finite element method (FEM) as implemented in commercial software (COMSOL Multiphysics®, v6.3, COMSOL AB, Stockholm, Sweden). For each age-specific geometry, a non-uniform computational mesh of triangular elements was generated, featuring strategic refinement near domain interfaces such as the trabecular meshwork and iris to ensure accurate field resolution.

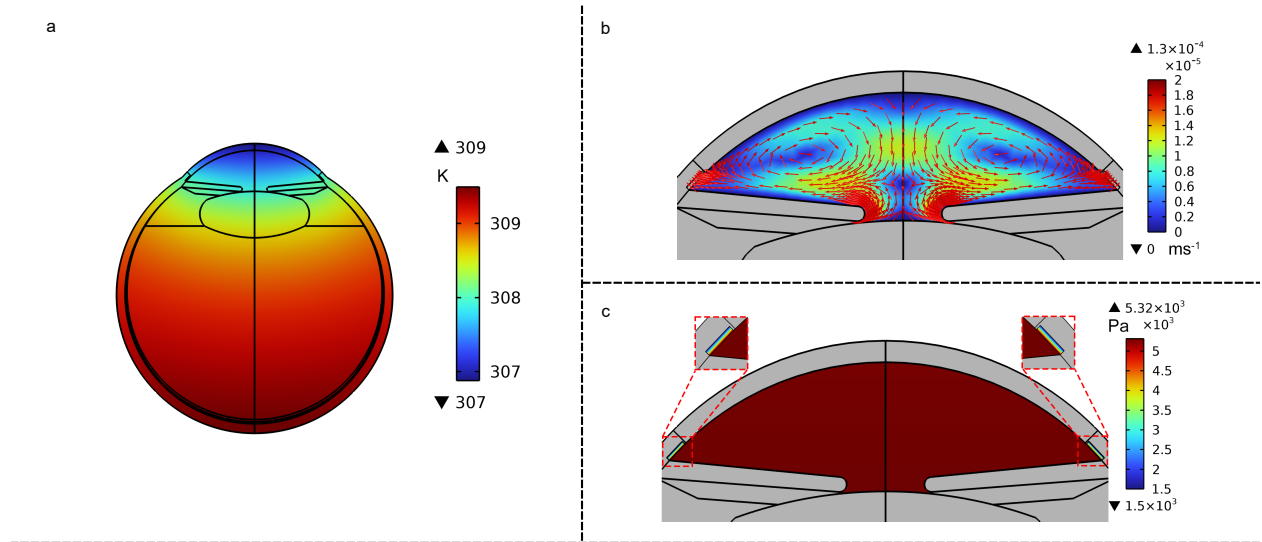
To ensure the results were independent of mesh discretization, a mesh convergence study was conducted for each geometry, with the steady-state IOP serving as the key convergence metric (Supplementary Table S5). The solution demonstrated excellent convergence, with the percentage difference in IOP between the finest mesh and the chosen mesh being less than 0.15% for all age groups. This mesh density was therefore used for the final simulation campaign. Robust steady-state solutions were obtained using the software’s fully coupled solver with the multifrontal massively parallel sparse (MUMPS) direct solver. A representative solution from the fully converged model is shown in Supplementary Figure S2. The figure illustrates the physically plausible temperature distribution, aqueous humor velocity field, and intraocular pressure gradient that form the basis

of our physics-informed training data. Notably, the pressure plot confirms the model correctly captures the significant pressure drop across the TM, which is the primary determinant of outflow resistance and IOP.

Table S5. Mesh convergence test for IOP.

Young			Middle			Old		
Domain Ele- ments	IOP (Pa)	% Diff	Domain Ele- ments	IOP (Pa)	% Diff	Domain Ele- ments	IOP (Pa)	% Diff
24,298	1741.2	-0.61%	24,202	1648.7	-0.81%	24,094	1614.5	-0.75%
27,480	1743.2	-0.49%	27,947	1655.1	-0.42%	27,745	1621.2	-0.34%
30,300	1744.4	-0.42%	31,461	1655.6	-0.39%	30,961	1621.3	-0.33%
38,600	1746.7	-0.29%	39,614	1658.0	-0.25%	39,326	1623.1	-0.22%
53,134	1749.7	-0.12%	52,930	1660.3	-0.11%	52,386	1625.2	-0.09%
89,196	1751.8	(Ref.)	82,102	1662.1	(Ref.)	81,270	1626.7	(Ref.)

Figure S2. Representative Multiphysics Solution from the Finite Element Model. **a**, Temperature distribution (K); **b**, Velocity field (m/s), with arrows indicating direction and color contours indicating magnitude; and **c**, Pressure field (Pa), showing the significant pressure drop across the trabecular meshwork (TM). This specific simulation corresponds to the following key input parameters: $K_{TM} = 5.00 \times 10^{-17} \text{ m}^2$; $Q_{AH} = 7.37 \times 10^{-11} \text{ m}^3/\text{s}$; $F_u = 3.36 \times 10^{-11} \text{ m}^3/\text{s}$; and $EVP = 1500 \text{ Pa}$, resulting in a calculated IOP = 5300 Pa (39.8 mmHg).



Supplementary Note 2: Sensitivity and Robustness to Physiological Priors

To assess the robustness of the framework’s outputs to the assumptions of the physiological priors, we performed two distinct sensitivity analyses on the full set of 38 measurements from the homogenous FMAT-1 cohort (Di Staso and Gaudio 2023). The results quantify the impact of varying prior distributions on the posterior median, coefficient of variation (CV), and the clinical risk classification derived from our inferred K_{TM} biomarker for each eye.

The first analysis tested sensitivity to prior uncertainty by re-running the full inference pipeline with the standard deviation (SD) of all priors increased (“Wide” scenario) or decreased (“Narrow” scenario) by 50%. The results (Supplementary Table S6, Part 1) show that the posterior medians of the core inferred biomarkers (K_{TM} , C_{trab}) are highly stable, while the posterior uncertainty (CV) responds rationally to the changes. The second analysis was a more stringent, out-of-distribution (OOD) stress test, where the mean of the Q_{AH} prior was shifted by an extreme margin of $\pm 30\%$ (“High Inflow” and “Low Inflow” scenarios). Even under these OOD conditions, the posterior median of the primary biomarker (K_{TM}) remains remarkably stable (Supplementary Table S6, Part 2).

Finally, the stability of the clinical diagnostic output was assessed for all scenarios. The results confirm that the risk classification based on the posterior median K_{TM} is perfectly stable against changes in prior uncertainty and remains highly robust ($>80\%$ stable) even when subjected to the OOD stress test (Supplementary Table S6, Part 3).

Supplementary Note 3: The Physics-Calibrated Data Scaling Strategy

To train the Stage 2 Patient-Specific Calibration Bridge, a massive, clinically-informed training dataset ($n=120,000$) was required to robustly capture patient-to-patient variability. Generating this dataset via direct high-fidelity simulation would be computationally intractable. We therefore developed and implemented our Physics-Calibrated Data Scaling (PCDS) strategy, a hybrid approach designed to create large-scale, physically-consistent datasets with a fraction of the computational cost.

The PCDS strategy involves three steps. First, we generate a large synthetic population using a computationally efficient surrogate model, the clinical Goldman equation. Second, to ensure physical consistency with our high-fidelity Finite Element (FE) model, we perform a planned calibration step. A representative subset of 500 parameter sets was run through both the FE model

Table S6. Robustness of framework outputs to variations in physiological priors. The framework’s inference pipeline was re-run on all 38 patient-condition pairs (19 untreated eyes and 19 steroid-treated fellow eyes) from the FMAT-1 cohort. Two separate sensitivity analyses were performed. The first test varied the prior uncertainty by increasing (“Wide”) or decreasing (“Narrow”) the standard deviation of all physiological priors by 50%. A second, out-of-distribution (OOD) test shifted the prior mean of only aqueous humor inflow (Q_{AH}) by $\pm 30\%$. The 3-part table below report (Part 1 and 2) the median percentage change in the posterior median and the posterior coefficient of variation (CV) for each biomarker, relative to the Baseline condition, and (Part 3) the stability of our inferred K_{TM} based clinical risk classification across all 38 eyes.

Part 1: Sensitivity to Prior Uncertainty (Standard Deviation Change)

Biomarker	Scenario	Median % Change in Posterior Median	Median % Change in Posterior CV
K_{TM}	Wide (+50% SD)	+6.37%	+35.52%
	Narrow (-50% SD)	-5.64%	-48.54%
C_{trab}	Wide (+50% SD)	+7.11%	+20.94%
	Narrow (-50% SD)	-9.20%	-32.90%
D_p	Wide (+50% SD)	+3.13%	+35.77%
	Narrow (-50% SD)	-2.86%	-48.09%
Q_{AH}	Wide (+50% SD)	+8.71%	+30.12%
	Narrow (-50% SD)	-5.73%	-45.93%
F_u	Wide (+50% SD)	-6.37%	+21.64%
	Narrow (-50% SD)	+19.69%	-45.17%
EVP	Wide (+50% SD)	+0.44%	+48.88%
	Narrow (-50% SD)	+0.17%	-50.27%

Conclusion: The posterior medians of core biomarkers (K_{TM} , C_{trab}) are highly stable (<10% change). The posterior uncertainty (CV) responds rationally to changes in prior uncertainty.

Part 2: Robustness to Out-of-Distribution Priors (Mean Change)

Biomarker	Scenario	Median % Change in Posterior Median	Median % Change in Posterior CV
K_{TM}	High Inflow (+30% Mean)	+9.76%	+3.07%
	Low Inflow (-30% Mean)	-6.86%	-5.33%
C_{trab}	High Inflow (+30% Mean)	+14.49%	+8.69%
	Low Inflow (-30% Mean)	-12.58%	-8.28%
D_p	High Inflow (+30% Mean)	+4.76%	+2.56%
	Low Inflow (-30% Mean)	-3.49%	-4.51%

Conclusion: Even under extreme out-of-distribution shifts in a key prior, the posterior median of the primary biomarker (K_{TM}) remains remarkably stable (<10% change).

Part 3: Clinical Classification Stability

Prior Test Scenario	Classification Stability
Wide Prior Uncertainty (+50% SD)	100% (38 out of 38 unchanged)
Narrow Prior Uncertainty (-50% SD)	100% (38 out of 38 unchanged)
High Inflow OOD (+30% Mean)	89.5% (34 out of 38 unchanged)
Low Inflow OOD (-30% Mean)	81.6% (31 out of 38 unchanged)

Conclusion: The framework’s clinical diagnostic output is perfectly stable against changes in prior uncertainty and remains highly robust (>80% stable) even when subjected to extreme out-of-distribution stress tests.

and the Goldman equation to quantify the known systematic biases between the models, as visualized in Supplementary Figure S3.

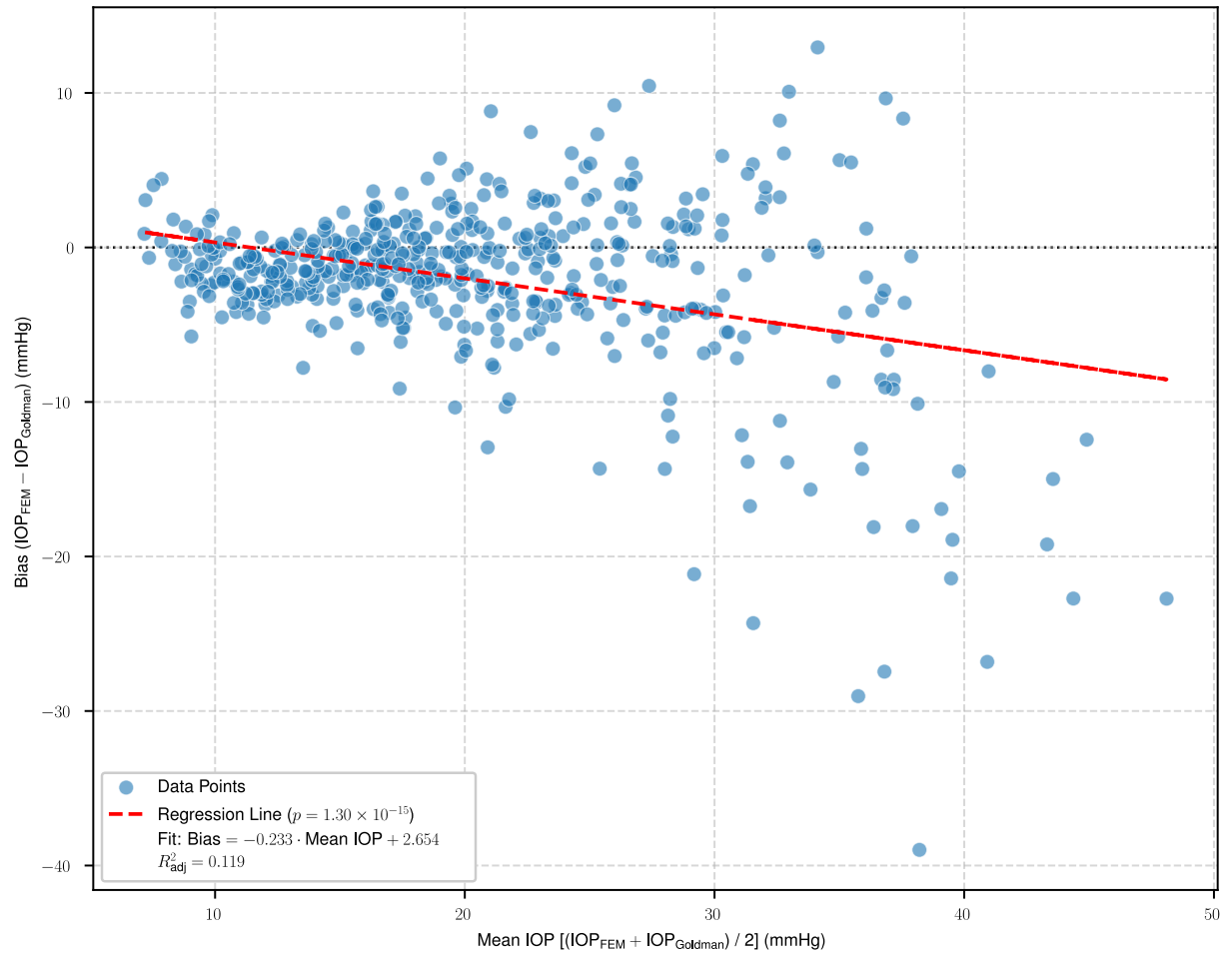
A linear regression analysis of these calibration data confirmed a statistically significant, pressure-dependent bias ($R^2_{\text{adj}} = 0.119$; $P < 10^{-14}$). The interpretation of these statistics is critical. The extremely low P -value, achieved with only 500 samples, provides overwhelming evidence that the detected linear trend is real and not an artifact of random chance, indicating sufficient statistical power. Conversely, the low R^2 value is an expected and direct consequence of our simulation design, visually apparent in the figure as a large degree of vertical scatter around a shallowly sloped regression line. This indicates that the variance of the systematic bias is small compared to the total variance, which is dominated by the intentionally introduced, high-variance simulated measurement noise (up to 3.5 mmHg SD). Therefore, the low R^2 does not signify a poor model fit but rather confirms that our analysis successfully identified a subtle but real systematic trend within a realistically noisy dataset. To further ensure the robustness of this trend, we also performed a Deming regression, which yielded a nearly identical intercept and slope, confirming the stability of the linear bias model.

The third and final step of PCDS is to apply a dynamic bias correction using the derived linear model:

$$\text{Bias}(\text{IOP}_{\text{Goldman}}) = 2.654 - 0.233 \times \text{IOP}_{\text{Goldman}} \quad (\text{S15})$$

This correction was applied to all 120,000 IOP values in the *in silico* dataset, creating a final, calibrated training set that is both computationally scalable and has improved physical consistency with our high-fidelity simulations.

Figure S3. Analysis of Bias Dependency between Physics Models. To ensure the physical consistency of the large-scale *in silico* dataset, we compared the IOP calculated by the high-fidelity finite element (FE) model against the simplified Goldman equation for a subset of 500 parameter sets. This plot shows the resulting bias ($\text{IOP}_{\text{FEM}} - \text{IOP}_{\text{Goldman}}$) as a function of the mean IOP. A linear regression revealed a statistically significant, pressure-dependent trend ($P < 10^{-14}$), confirming a systematic bias between the two models.



Supplementary Note 4: Machine Learning Model Performance and Hyperparameters

To ensure full transparency and reproducibility, this section details the final performance metrics and optimized hyperparameters for the machine learning models used in our two-stage framework. The performance of all models was evaluated on a held-out test set, representing 20% of the respective dataset, that was not used during training or hyperparameter tuning. A full suite of

diagnostic tests was performed for both AI stages, with the results detailed in Figure S4

Model Performance Comparison

The selection of XGBoost for the Stage 1 task was based on a comprehensive comparison against other standard regression algorithms. While Random Forest showed marginally higher R-squared, the overall performance of the XGBoost model was deemed superior for this application. Table S7 summarizes the key performance metrics for the evaluated models, demonstrating the strong performance of the final, tuned XGBoost regressors for both stages of the framework.

Table S7. Performance Comparison of Machine Learning Models. Performance metrics were evaluated on the held-out test set for the Stage 1 (K_{TM}) and Stage 2 (G -factor) prediction tasks. All metrics are reported on the \log_{10} -transformed scale of the respective target variable unless otherwise noted.

Model	R-squared	RMSE
<i>Stage 1: K_{TM} Prediction Task</i>		
Random Forest (Tuned)	0.775	0.269
XGBoost (Tuned, Final)	0.770	0.272
Linear Regression	0.593	0.362
<i>Stage 2: G-factor Prediction Task</i>		
XGBoost (Final)	0.790	0.126

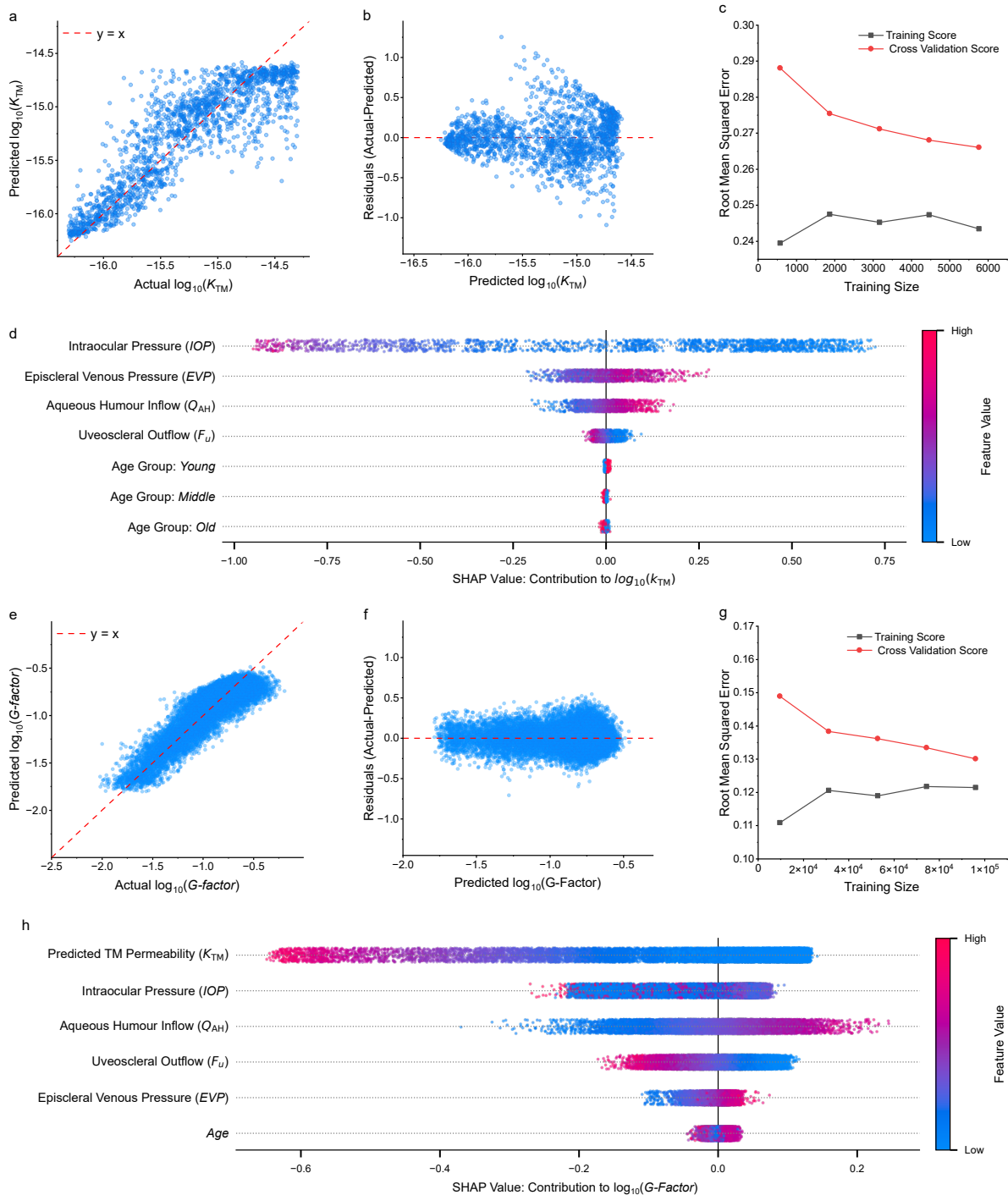
Optimized Hyperparameters

The final hyperparameters for the selected models were determined using a 5-fold cross-validated, randomized search procedure. The final, optimized parameters used to build the production models are detailed in Table S8.

Table S8. Final Optimized Hyperparameters. The table lists the specific hyperparameters for the final, trained XGBoost models used in the framework.

Hyperparameter	Stage 1 Model (K_{TM})	Stage 2 Model (G -factor)
n_estimators	425	491
learning_rate	0.0851	0.1731
max_depth	12	3
subsample	0.7307	0.8645
colsample_bytree	0.9356	0.5994
gamma	0.4302	0.0028
reg_alpha	0.3033	—
reg_lambda	0.5371	—

Figure S4. Performance and interpretability of the two-stage AI. **a-d**, Diagnostic evaluation of the Stage 1 AI model for permeability (K_{TM}) prediction, showing: **a**, predicted vs. actual performance ($R^2 = 0.77$); **b**, a residual plot; **c**, the model learning curve; and **d**, a SHAP summary plot of feature importance. **e-h**, Diagnostic evaluation of the Stage 2 AI model for geometric factor (G) prediction, showing: **e**, predicted vs. actual performance ($R^2 = 0.79$); **f**, a residual plot; **g**, the model learning curve; and **h**, a SHAP summary plot confirming the transfer of information from Stage 1.



Supplementary Note 5: Comprehensive Statistical Validation of C_{trab} Agreement

To rigorously quantify the agreement between the framework's non-invasive C_{trab} estimate (posterior median) and the measured outflow facility (OF) from the FMAT-1 cohort (n=19 paired eyes), we performed a comprehensive statistical validation. Standard Bland-Altman analysis was supplemented with advanced statistical techniques to fully characterize the method's performance and the precision of the validation results, particularly given the cohort size.

Table S9. Comprehensive statistical validation of C_{trab} agreement.

Metric	Condition	Value	95% Bootstrap CI	Interpretation
Spearman's Rho (ρ)	Untreated	0.938	[0.810, 0.989]	Excellent Correlation
	Steroid	0.946	[0.835, 0.989]	Excellent Correlation
ICC(2,1)	Untreated	0.918	[0.690, 0.970]	Excellent Reliability
	Steroid	0.881	[0.670, 0.960]	Good to Excellent Reliability
Bias (Mean Diff.) ($\mu\text{L}/\text{min}/\text{mmHg}$)	Untreated	0.011	[0.004, 0.018]	Clinically Negligible Bias
	Steroid	-0.014	[-0.024, -0.003]	Clinically Negligible Bias
SD of Differences ($\mu\text{L}/\text{min}/\text{mmHg}$)	Untreated	0.016	[0.010, 0.020]	High Precision
	Steroid	0.024	[0.017, 0.029]	High Precision
Lower LoA ($\mu\text{L}/\text{min}/\text{mmHg}$)	Untreated	-0.020	[-0.032, -0.005]	Tight Agreement
	Steroid	-0.061	[-0.072, -0.044]	Tight Agreement
Upper LoA ($\mu\text{L}/\text{min}/\text{mmHg}$)	Untreated	0.043	[0.031, 0.052]	Tight Agreement
	Steroid	0.033	[0.013, 0.048]	Tight Agreement
Within-Subject SD (S_w) ($\mu\text{L}/\text{min}/\text{mmHg}$)	Untreated	0.047	N/A	Typical Single-Point Uncertainty
	Steroid	0.041	N/A	Typical Single-Point Uncertainty
Prop. $ \text{Diff} > 0.05$ ($\mu\text{L}/\text{min}/\text{mmHg}$)	Untreated	31.9%	N/A	Expected Error Rate
	Steroid	32.4%	N/A	Expected Error Rate

Note: CI, Confidence Interval; ICC, Intraclass Correlation Coefficient; LoA, Limits of Agreement. *Prop. $|\text{Diff}| > 0.05$* represents the average proportion of posterior estimates that deviated from the measured value by more than a clinical threshold of $0.05 \mu\text{L}/\text{min}/\text{mmHg}$. 95% CIs for Spearman's Rho, ICC, Bias, SD, and LoA were calculated using a non-parametric bootstrap with 1,000 resamples.

The full results are detailed in Supplementary Table S9. The analysis was performed separately

for the Untreated and Steroid-treated conditions. Spearman’s rank correlation (ρ) was used to assess the monotonic relationship between the estimated and measured values. Intraclass Correlation Coefficient (ICC(2,1)) was calculated to evaluate absolute agreement and reliability. Standard Bland-Altman analysis was used to determine the mean difference (bias) and the 95% limits of agreement (LoA).

To quantify the uncertainty of these agreement and correlation statistics, we employed a non-parametric bootstrap procedure (1,000 resamples). By repeatedly resampling the 19 patient pairs with replacement, we generated 95% confidence intervals (CIs) for the Spearman’s ρ , ICC, bias, and LoA values.

Finally, two additional metrics were calculated to provide further insight. The Within-Subject Standard Deviation (S_w) was computed as the average standard deviation of the 1,000-sample posterior distribution of the difference for each of the 38 patient-condition pairs, representing the typical predictive uncertainty for a single measurement. The proportion of differences exceeding a clinical threshold of 0.05 $\mu\text{L}/\text{min}/\text{mmHg}$ was calculated to provide a clinically interpretable measure of the expected error rate.

Supplementary Note 6: Assignment of Ground-Truth Risk Labels for the Heterogeneous Validation Set

To validate the classification performance of the K_{TM} -based risk thresholds, a ground-truth risk label (Normal, Borderline, or Compromised) was assigned to each of the 27 cohorts in our heterogeneous validation set. The assignment was performed using the following pre-specified, systematic rule-based system based on the cohort’s description in its source publication:

1. Normal: Cohorts explicitly described as “Healthy” or “Normal Controls.”
2. Compromised (by Diagnosis): Cohorts with a definitive diagnosis of “Primary Open-Angle Glaucoma (POAG),” “Open-Angle Glaucoma (OAG),” or “Glaucoma.”
3. Borderline: Cohorts described as having only “Ocular Hypertension (OHT).”
Exception: If the cohort’s reported mean outflow facility was exceptionally low ($\text{OF} \leq 0.10 \mu\text{L}/\text{min}/\text{mmHg}$), the label was escalated to Compromised.
4. Mixed Cohorts: For cohorts containing a mix of OHT and POAG patients, a Compromised label was assigned if the described proportion of diagnosed glaucoma patients was greater than or equal to 25% ($\geq 25\%$). For cohorts with ambiguous descriptions, a conservative label of Borderline was applied.

The application of these rules to each of the 27 clinical cohorts is detailed in Supplementary Table S10 below.

Table S10. Summary of Ground-Truth Label Assignment for the Heterogeneous Validation Set. This table summarizes the application of the rule-based system described in Supplementary Note 4 to each of the 27 clinical cohorts. The full curated dataset, including all cohort characteristics and summary statistics, is available at the public repository cited in Section 5

ID	Source Study	Group Description	Justification / Rule Applied	Label
1	Toris et al. (2002)	Healthy Controls (Normotensive)	Rule 1: Described as “Healthy”	N
2	Toris et al. (2002)	OHT	Rule 3: OHT, OF > 0.10	B
3	Toris et al. (2004)	Mixed POAG/OHT Baseline	Rule 3 (Exception): Primarily OHT, but OF ≤ 0.10	C
4	Toris et al. (1999)	Young Healthy Baseline	Rule 1: Described as “Healthy”	N
5	Toris et al. (1999)	Old Healthy Baseline	Rule 1: Described as “Healthy”	N
6	Sit et al. (2021)	POAG/OHT Baseline	Rule 4: Mixed, POAG % = 25% ($\geq 25\%$)	C
7	Gulati et al. (2017)	Mixed POAG/OHT Baseline (Pre-SLT)	Rule 4: Mixed, POAG % = 89.7% ($> 25\%$)	C
8	Alaghband et al. (2019)	Healthy Control	Rule 1: Described as “Healthy”	N
9	Sit et al. (2008)	Healthy Baseline	Rule 1: Described as “Healthy”	N
10	Meyer et al. (1997)	Cataract Patients (Low Outflow Facility)	Rule 4: Ambiguous, “Low C” indicates risk	B
11	Liu et al. (2011)	Healthy Baseline	Rule 1: Described as “Healthy”	N
12	Hayashi et al. (1989)	OHT Baseline	Rule 3: OHT, OF > 0.10	B
13	Fernandez-Barrientos et al. (2010)	Mixed OHT/POAG (Pre-Cataract Surgery)	Rule 4: Mixed, POAG % = 90.9% ($> 25\%$)	C
14	Kazemi et al. (2019)	Healthy Controls (Baseline)	Rule 1: Described as “Healthy”	N
15	Hays et al. (2014)	Ex Vivo Human Donor Eyes (Baseline)	Rule 1: Assumed healthy donor eyes	N
16	Goyal et al. (2010)	Mixed POAG/OHT (180° SLT Group, Baseline)	Rule 4: Mixed, POAG % = 67% ($> 25\%$)	C
17	Goyal et al. (2010)	Mixed POAG/OHT (360° SLT Group, Baseline)	Rule 4: Mixed, POAG % = 79% ($> 25\%$)	C
18	Saito et al. (2001)	POAG (Pre-Treatment Baseline)	Rule 2: Described as “POAG”	C
19	Johnson et al. (2010)	OHT Baseline	Rule 3: OHT, OF > 0.10	B

Continued on next page

Table S10 – *Continued*

ID	Source Study	Group Description	Justification / Rule Applied	Label
20	Gulati et al. (2012)	OHT Baseline	Rule 3: OHT, OF > 0.10	B
21	Costagliola et al. (1995)	POAG Only Baseline (Normotensive)	Rule 2: Described as “POAG”	C
22	Beltran-Agullo et al. (2011)	POAG/OHT (White Caucasian)	Rule 4: Mixed, POAG % = 44% (> 25%)	C
23	Beltran-Agullo et al. (2011)	Healthy Controls (White Caucasian)	Rule 1: Described as “Healthy”	N
24	Minckler et al. (2005)	OAG (Post-Washout Baseline)	Rule 2: Described as “OAG”	C
25	Grieshaber et al. (2010)	POAG (Black African Cohort)	Rule 2: Described as “POAG”	C
26	Pandey and Sujata (2014)	POAG (Beta-Blocker Group, Baseline)	Rule 2: Described as “POAG”	C
27	Pandey and Sujata (2014)	POAG (Non-Beta-Blocker Group, Baseline)	Rule 2: Described as “POAG”	C

Abbreviations: N, Normal; B, Borderline; C, Compromised.